Available online at www.sciencedirect.com

SciVerse ScienceDirect

Geochimica et Cosmochimica Acta 112 (2013) 66–86

Geochimica et Cosmochimica Acta

www.elsevier.com/locate/gca

Texture-specific isotopic compositions in 3.4 Gyr old organic matter support selective preservation in cell-like structures

Kevin Lepot [a,b,*], Kenneth H. Williford [a,c], Takayuki Ushikubo [a], Kenichiro Sugitani [d], Koichi Mimura [e], Michael J. Spicuzza [a], John W. Valley [a]

[a] NASA Astrobiology Institute, WiscSIMS, Department of Geoscience, University of Wisconsin, 1215 W. Dayton St., Madison, WI 53706, USA
[b] Université Lille 1, Laboratoire Géosystèmes, CNRS UMR8217, 59655 Villeneuve d'Ascq, France
[c] Jet Propulsion Laboratory, 4800 Oak Grove Dr., Pasadena, CA 91109, USA
[d] Department of Environmental Engineering and Architecture, Graduate School of Environmental Studies, Nagoya University, Nagoya 464-8601, Japan
[e] Department of Earth and Environmental Sciences, Graduate School of Environmental Studies, Nagoya University, Nagoya 464-8601, Japan

Received 12 October 2012; accepted in revised form 4 March 2013; Available online 14 March 2013

Abstract

Abundant cell-like organic structures have been proposed as microfossils in Paleoarchean (3.2–3.5 Ga) cherts. The wide range of $\delta^{13}C_{org}$ values recorded in Paleoarchean organic matter (OM), including some of these possible microfossils, is difficult to reconcile with the smaller range observed in living cells and younger microfossils. Metamorphic and metasomatic effects on $\delta^{13}C_{org}$ have been recognized in Paleoarchean rocks, but have never been assessed for cell-like structures. Migrations of OM, of which the textures can mimic microfossils, are also difficult to constrain in Paleoarchean cherts that are often cut by submillimeter- to meter-scale OM-bearing veins.

Here, we present the results of petrography, Raman microspectroscopy, and in situ analyses of $\delta^{13}C_{org}$ and H/C using secondary ion mass spectrometry (SIMS) of diverse organic microstructures, including possible microfossils, from two localities of the 3.4-billion-year-old Strelley Pool Formation (Western Australia, SPF). For the first time, we show that the wide range of $\delta^{13}C_{org}$ values recorded at the micrometer scale correlates with specific OM-texture types in the SPF. The cross-cutting texture and lower structural order show that the OM in micro-veins of one sample from the Goldsworthy greenstone belt (WF4) post-dates all other OM-texture types. Possible microfossils (spheres, lenses), clots and micrometer-scale globules all show a higher structural order reached during peak metamorphism. Other than late micro-veins, textures indicative of OM migration beyond the millimeter-scale are absent; hence the source of clots, lenses, spheres and globules is indigenous to the cherts. A weak positive relation between $\delta^{13}C_{org}$ and H/C demonstrates that the 10‰ range in $\delta^{13}C_{org}$ recorded in indigenous OM is not metamorphic or metasomatic in origin. Texture-specific isotopic compositions strongly argue against fully abiotic OM synthesis. Spherical cell-like structures have distinct $\delta^{13}C_{org}$ values compared to all other organic textures: their distribution peaks between −35‰ and −36‰ in WF4 and averages −35.7‰ in sample PAN1-1A from the Panorama greenstone belt. Lenses are composed of a network of nanoscale OM with a relatively high H/C and $\delta^{13}C_{org}$ (average −32‰ in WF4), and include globules with lower H/C and $\delta^{13}C_{org}$ down to −40‰. Similar globules also appear as isolated clusters. In both WF4 and PAN1-1A, $\delta^{13}C_{org}$ of OM clots shows a bimodal distribution, the lower values overlapping with those of lenses. These heterogeneities can be explained by different carbon-fixation metabolisms, e.g. photosynthetic high $\delta^{13}C_{org}$ lenses *versus* methanogenic low $\delta^{13}C_{org}$ spheres. Alternatively, heterogeneities can be explained by selective diagenetic

Abbreviations: OM, organic matter; SPF, Strelley Pool Formation; SIMS, secondary ion mass spectrometry; BSE, backscattered electrons; SE, secondary electrons; $\delta^{13}C_{org}$, organic carbon isotope fractionation in ‰ relative to Vienna Pee Dee Belemnite (VPDB)

* Corresponding author at: Université Lille 1, Laboratoire Géosystèmes, CNRS UMR8217, bâtiment SN5, 59655 Villeneuve d'Ascq, France. Tel.: +33 320434921.

E-mail address: kevin.lepot@univ-lille1.fr (K. Lepot).

http://dx.doi.org/10.1016/j.gca.2013.03.004

preservation of the distinct isotopic fractionations inherited from different precursor biomolecules. Selective preservation is supported by (i) coupled $\delta^{13}C_{org}$–H/C heterogeneities, (ii) the $\delta^{13}C_{org}$ differences between cell-like structures and recondensed clots, (iii) internal isotopic heterogeneities in SPF lenses similar to heterogeneities in modern and fossil cells. These results support the interpretation of biogenicity of morphologically cellular structures in the SPF.

1. INTRODUCTION

The oldest evidence of life comes from Paleoarchean rocks and the 3.4 Ga Strelley Pool Formation (SPF) contains what may be the best preserved and most diverse record of life from this time, including stromatolites and diverse cell-like microstructures. The biogenicity of the SPF carbonate stromatolites is strongly implied by the link between morphology, organic matter (OM) distribution and sedimentary environments (Allwood et al., 2006a, 2009). Sulfur isotopes indicate sulfur-based metabolism before 3.4 Ga (Philippot et al., 2007; Ueno et al., 2008; Shen et al., 2009; Wacey et al., 2010; Bontognali et al., 2012; McLoughlin et al., 2012). Paleoarchean rocks preserve the oldest amorphous OM that is rich in organic functional groups (Marshall et al., 2007; Derenne et al., 2008), unlike older rocks where graphitization has removed the organic functionality and progressively re-organized the macromolecular OM to a regularly stacked graphitic structure (Papineau et al., 2010). However, most Paleoarchean rocks are characterized by the geochemical imprint of syn-sedimentary or metasomatic hydrothermal fluids (Allwood et al., 2010; Yamaguchi et al., 2011).

Hydrothermal reactions can form organic compounds (McCollom and Seewald, 2006). Thus, the presence of a mafic basement favoring serpentinization and associated abiogenic OM synthesis, and the occurrence of abundant carbon-bearing hydrothermal veins have raised the question, could some Palaeoarchean OM be abiogenic (Brasier et al., 2002; Lindsay et al., 2005)? The ranges of carbon isotope fractionation observed in Paleoarchean methane-bearing fluid inclusions and kerogen (Ueno et al., 2004, 2006a) can be produced by abiotic synthesis and have thus been debated as a biosignature (McCollom and Seewald, 2006; Sherwood Lollar and McCollom, 2006; Ueno et al., 2006b). Long aliphatic chains with biogenic imprints have been found in Paleoarchean kerogen (Derenne et al., 2008), although the exceptional preservation of such fragile molecules in sub-greenschist metamorphosed rocks raised questions about their origin (Marshall et al., 2007). Strong similarities have been shown between molecular profiles in the SPF cherts and Mesoproterozoic biogenic kerogen, nevertheless, the authors conclude that abiogenic kerogen remains to be studied using the same approach in order to use these profiles as definitive biosignatures (Marshall et al., 2007).

Abundant possible organic-walled microfossils have been reported in Mesoarchean to Palaeoarchean rocks, but migration of OM along quartz grain boundaries forming cell-like abiogenic microstructures is still difficult to rule out. The 3.5 Ga Apex chert (Australia) OM filaments, initially reported as the oldest bacterial microfossils (Schopf, 1993), have come under close scrutiny. It has been shown that these filaments occur in a massive OM-rich chert vein (Brasier et al., 2002) that was submitted to intense hydrothermal and groundwater alteration (Pinti et al., 2009b), where filamentous pseudomicrofossils formed in microveins (Marshall et al., 2011). Filamentous structures belong to a morphological continuum with variable filament diameters, branching structures, and association with some crystal pseudomorphs, leading to their interpretation as the result of OM migration along crystal boundaries (Brasier et al., 2005). Synthetic mineral templates have been proposed as candidates for filamentous OM aggregation (Garcia-Ruiz et al., 2003). 2D–3D Raman mapping and scanning laser-confocal microscope imaging of some Apex chert filaments (Schopf et al., 2002; Schopf and Kudryavtsev, 2012) nevertheless show that the filamentous OM textures are more complex than linear grain-boundary coatings and triple-junction fillings, and consistent with what is observed in younger microfossils (Kazmierczak and Kremer, 2009).

Abundant newly discovered microfossils have been recently reported in rocks older than 3.0 Ga. Siliciclastic rocks of the 3.2 Ga Moodies Group (South Africa) (Javaux et al., 2010) and the 3.0 Ga Farrel Quartzite cherts (Australia) (Sugitani et al., 2007; Grey and Sugitani, 2009) yielded integral cell-wall-like OM through acid-mediated extraction, a feature only known from microfossils. The 3.0 Ga Farrel Quartzite OM includes spheres and flanged lenses (formerly named "spindles") that exhibit bounding-wall morphologies and degradation textures consistent with those of accepted fossil cells (Sugitani et al., 2007; Schopf et al., 2010).

Silicified sediments of the 3.4 Ga SPF (Sugitani et al., 2010, 2013; Wacey et al., 2011, 2012) show abundant microstructures of OM, including clots, films, filaments, and cell-like structures (spheres, flanged and non-flanged lenses, microtubes) bound by organic walls. To the best of our knowledge, no mineral template occurring in nature mimics the lenses (Sugitani et al., 2010), large ovoids, and microtubular sheaths (Wacey et al., 2011) of the SPF. Moroever, Wacey et al. (2011, 2012) have shown that the morphology of some SPF spherical microstructures is consistent with that of younger microfossils down to the nanoscale, including the presence of silica nanospheres at the boundary of and within the organic wall. In the same rock, these authors have shown that spherical structures formed by aggregation of migrated carbon along grain boundaries of botryoidal quartz display wall-like OM microstructures, a common feature of organic-rich cherts (Buick, 1990). Thus, although not all abiotic structures have been critically studied so far, nanoscale petrography can provide textural constraints to better distinguish microstructures resulting of OM migration and those that are consistent with cells.

Nanoscale co-distributions of C, N, and S provide additional constraints for the origin of 3.0 Ga (Oehler et al., 2010) and 3.4 Ga (Wacey et al., 2011) cell-like structures, although the presence of heteroatoms alone is not proof of biogenicity. Nitrogen-, oxygen-, and hydrogen-bearing molecules may form abiotically (Horita, 2005), and heteroatoms such as sulfur may be added abiotically to OM (Sinninghe Damste et al., 1998; Lepot et al., 2009). More promising are heterogeneities in heteroatom contents between different OM textures at small scale suggesting different precursor molecules. For example, associated filamentous and spherical Proterozoic microfossils show distinct N/C ratios (Oehler et al., 2006). The Farrel Quartzite (3.0 Ga) lenses often display dense, ca. 1 μm wide OM globules enriched in sulfur and nitrogen compared to the reticulate OM network forming the body of the cell-like structure (Oehler et al., 2010).

The association of isotopically fractionated pyrite sulfur with putative microfossils has been used to propose that the majority of preserved microfossils in a SPF sandstone represent S-metabolizing microbes (Wacey et al., 2011). Nanoscale pyrites are indeed associated with OM within and near arcuate shapes interpreted as partial cell walls, and larger pyrite grains occur near spherical cell-like structures (Wacey et al., 2011). Several lines of evidence restrict the genesis of these features. First, the microfossil origin of the arcuate forms associated with nano-pyrites remains dubious. Unlike spherical cell-like structures (Wacey et al., 2011, 2012), these arcuate forms show a highly discontinuous OM wall at the nanoscale, a feature the authors also found in OM-coated abiotic botryoids. In our view, additional nanoscale petrography is required to constrain the origin of these pyrite-associated microstructures. Second, alternative abiogenic sources have been proposed for such large $\delta^{34}S$ and $\Delta^{33}S$ values (Philippot et al., 2012), and $\delta^{36}S$ measurements are important to confirm Archean S-metabolism (Ueno et al., 2008; Shen et al., 2009). Finally, metabolically fractionated sulfur isotope ratios in pyrite are consistent with, but not conclusive proof that nearby fossil microorganisms metabolized sulfur. OM is often the preferred locus of pyrite precipitation away from or without preservation of the bacteria that mediated pyrite precipitation, e.g. at grain boundaries together with clotted kerogen (Lepot et al., 2009), or within fossil plants (Bernard et al., 2010a). Moreover, no SIMS instrument has achieved so far the spatial resolution to accurately analyze the sulfur isotope ratio in nano-pyrites within organic walls, and thus existing studies could only target larger pyrites in the immediate vicinity (Wacey et al., 2010).

A wide range of $\delta^{13}C_{org}$ was measured by SIMS analysis of possible microfossils in the SPF (−46‰ to −33‰) (Wacey et al., 2011) and older rocks (−42‰ to −32‰) (Ueno et al., 2001), but such values can be the result of a range of biotic (Pearson, 2010) and abiotic (McCollom and Seewald, 2006) processes. In those studies, no links between $\delta^{13}C_{org}$, the different OM microstructures and cell-like morphologies were evidenced. In contrast, the $\delta^{13}C_{org}$ values of Proterozoic microfossils: (i) typically display ranges of ~5‰ for individual taxa, although some show larger range (House et al., 2000; Kaufman and Xiao, 2003; Orphan and House, 2009; Williford et al., 2013), and (ii) can be correlated with morphological (taxonomic or anatomic) features (Williford et al., 2013).

Several processes can explain $\delta^{13}C_{org}$ heterogeneities at different scales, including: (1) microbial metabolism (Pearson, 2010), (2) possibly, abiotic synthesis (McCollom and Seewald, 2006), (3) preservation of different classes of molecules with distinct biosynthetic $\delta^{13}C_{org}$ (Hayes, 2001), (4) different diagenetic conditions (Galimov, 2006), (5) differential hydrothermal or metamorphic alteration (Dunn and Valley, 1992; Des Marais, 2001; Valley, 2001), and (6) migration of OM with distinct $\delta^{13}C_{org}$ (Williford et al., 2011a). On a regional scale, OM in ca. 3.5 Ga massive veins and Paleoarchean sediments shows variable $\delta^{13}C_{org}$ that has been interpreted as resulting from differential metamorphic conditions based on correlation with bulk OM content (Ueno et al., 2004), N/C ratios (van Zuilen et al., 2007), and N-isotopes and metal concentrations (Pinti et al., 2009a). Paleoarchean oil migration is known at least in some initially porous rocks (sandstones/siltstones) (Buick et al., 1998), and different generations of OM have been distinguished by Raman microspectroscopy in the Apex chert (Olcott Marshall et al., 2012). In the SPF, a relatively wide range of bulk-rock $\delta^{13}C_{org}$ has been observed both in massive veins (−34‰ to −26.9‰) and sediments (−35.8‰ to −28.3‰) (Lindsay et al., 2005; Marshall et al., 2007), and the origin of OM in sediments remains unclear. Wacey et al. (2011) demonstrated that OM in the SPF sandstones is indigenous because it mostly occurs: (1) in specific sandstone layers, and (2) in the earliest isopachous cement. So far, in situ $\delta^{13}C_{org}$ analyses have only targeted cell-like OM in some Paleoarchean rocks (Ueno et al., 2001; Wacey et al., 2011), and migrated OM in others (van Zuilen et al., 2007). Coupled petrographic and in situ geochemical analyses of all OM textures in Paleoarchean rocks are thus crucial to constrain questions of biogenicity and genesis of OM.

We have thoroughly analyzed the textures, distribution and structure of diverse OM microstructures in cherts of the SPF using Raman microspectroscopy, optical and electron microscopy, and performed in situ SIMS isotopic analyses on each OM-texture type. This study provides unprecedented insights into formation, origin of cell-like structures, migration, and alteration of OM in the SPF.

2. GEOLOGIC SETTING AND SAMPLES

The SPF formed ~3.35 Ga ago and crops out across eleven greenstone belts in the Pilbara Craton (Hickman, 2008). It is part of the Pilbara Supergroup, unconformably overlies the Warrawoona Group, and is overlain by the Euro Basalt. We studied (Supplementary Figs. S1–S4) a massive to layered black chert (WF4) and a stromatolitic chert (WFL2-1) from the Goldsworthy greenstone belt (Sugitani et al., 2010), and a laminated black chert from the Panorama greenstone belt (PAN1-1A). The two sampled localities are ca. 100 km from each other. WF4 and WFL2-1 were sampled at the informally named Water Fall ridge in the north of Mount Grant quadrangle in the Goldsworthy greenstone belt. There, the sedimentary succession

of the SPF comprises quartz-rich sandstones interbedded with massive to laminated chert beds as well as stromatolitic cherts (Sugitani et al., 2007, 2010; Hickman, 2008). The Water Fall ridge samples (WF4 and WFL2-1) come from the uppermost cherty unit ca. 2 m thick of shallow water origin that consists of sandstones, conglomerate, parallel laminated cherts, stromatolitic chert, and massive chert at the top. The massive WF4 chert was collected at the center of the ridge (S20°20′40″, E119°25′09″). The stromatolitic WFL2-1 chert is stratigraphically lower than WF4, and laterally 50 m away from the massive WF4 chert. REE+Y compositions suggest a hydrothermal contribution to the formation of the WF4 chert (Yamaguchi et al., 2011). PAN1-1A was sampled at the unnamed ridge (S21°13′21″, E119°18′20″) in the Panorama greenstone belt, near the southern margin of the 'Trendall Ridge'. The laminated PAN1-1A chert comes from a sedimentary unit deposited in peritidal to inner platform environment (Sugitani et al., 2013). The REE+Y compositions of laterally equivalent cherts close to the 'Trendall Locality' also suggest precipitation of chert from mixed marine-hydrothermal fluids (Allwood et al., 2010).

3. METHODS

3.1. Microscopy

Optical petrography was carried out using an Olympus BX51 microscope under bright-field transmitted light and reflected light. Photomicrographs from different focal planes were combined into "multiplane images" using a weighted average algorithm (CombineZP software by Alan Hadley). Optical cathodoluminescence was carried out using a Technosyn Cold Cathode Luminescence 8200 MK4 (electron gun operated at 25.4 kV, 460 μA) coupled to an Olympus BX41 microscope. SEM images were recorded on gold-coated samples using a Hitachi S3400 SEM (at UW-Madison) operated at 10–15 kV and a working distance of 10 mm. Secondary electron (SE) images were recorded before SIMS analyses, and show OM in black, quartz in gray, sulfides in white and topographic relief outlined by white halos. Backscattered electron images (BSE) were recorded after SIMS analyses, removal of the gold coating and deposition of a ca. 10-nm-thick gold coat. BSE images show OM in black, quartz in gray; sulfides and the remains of the earlier gold coat within topography appear in white.

3.2. Raman spectromicroscopy

Raman spectra were obtained with a Jobin Yvon Labram spectrometer (at Université Lille 1) with a 514.5 nm Spectra Physics argon laser (vertical polarization) focused through an Olympus BX40 microscope with a 100× objective (NA = 0.9) into a spot 1–2 μm large. Measured laser power at the sample surface was less than 7 mW and prevented heat-induced artifacts. Raman spectra were recorded on carbonaceous particles located below the surface of polished thin sections to avoid artifacts caused by the polishing process. The backscattered Raman signal was dispersed by a grating (1800 lines/mm) and analyzed with a front-illuminated CCD detector. Baseline subtraction was performed in Labspec using a cubic interpolation with six fixed points (800, 950, 1100, 1710, 1830, 2000 cm^{-1}).

3.3. Bulk carbon isotope analyses

The $\delta^{13}C_{org}$ of bulk insoluble OM in PAN1-1A was measured using conventional extraction techniques as detailed in Supplementary methods and (Kitchen and Valley, 1995). The $\delta^{13}C_{org}$ of bulk insoluble OM of WF4 was reported in Sugitani et al. (2010), and that of WFL2-1 (unpublished) was measured by these authors using the method reported therein.

3.4. SIMS measurements

SIMS analyses of carbon isotope ratios were carried out using a CAMECA IMS-1280 at the WiscSIMS laboratory, UW-Madison (Valley and Kita, 2009), following the procedure described in Williford et al. (2013). Sample preparation is described in Supplementary methods. A ~15 μm (~7 μm for 4 analyses of lenses in WF4) $^{133}Cs^{+}$ primary ion beam with 20 kV total accelerating voltage and ~2.5 nA intensity was focused at the sample surface. Secondary ions were counted simultaneously using the following detector setup: $^{12}C^{-}$ (Faraday cup at the L′2 position with a 10^{11} Ω resistor, mass resolution $M/\Delta M = 2200$), $^{13}C^{-}$ [axial electron multiplier (EM), $M/\Delta M = 4000$], and $^{13}CH^{-}$ (EM at the H2 position, $M/\Delta M = 2200$). Deflector X and Y parameters (DTFA) were adjusted by rastering the primary beam over a 25 × 25 μm area near each target area and applying the dynamic transfer plate voltage synchronized with primary beam rastering to obtain a stable secondary ion image. Values of $\delta^{13}C_{Raw}$ (in ‰) represent the $^{13}C/^{12}C$ isotopic ratio measured by SIMS reported against the VPDB value before correction for instrumental bias (Supplementary methods and Fig. S5). Each analysis consisted of 70 s of presputtering and 80 measurement cycles of 2 s each. Instrumental bias in SIMS was standardized using an epoxy-embedded chip of carbonaceous chert sample PPRG-215-1 (Walter et al., 1983) provided by C.H. House, the same standard used by House et al. (2000) and Williford et al. (2013) for $\delta^{13}C$ measurements of Precambrian microfossils. Bias (α_{SIMS}) was calculated by comparing the average "raw" value of PPRG-215-1 to the published value [-31.5 ± 0.2‰ VPDB (Hayes et al., 1983; House et al., 2000)], as detailed in Supplementary methods and (Kita et al., 2009; Valley and Kita, 2009). The last three analyses of PAN1-1A were similarly standardized using the WFL2-1 stromatolitic chert after demonstration of its $\delta^{13}C_{org}$ homogeneity (see below). Calculations of the internal and external precisions, as well as the resulting *analytical uncertainty* that we report in all figures herein, are detailed in Supplementary methods. PPRG-215-1 was located on a different mount than SPF samples. Supplementary methods, Figs. S6–S8 and previous studies (Kita et al., 2009; Ferry et al., 2010) indicate that off-mount calibration with a sample change from the high-vacuum airlock chamber, variations of analysis-

chamber pressure and sample coordinates do not modify bias on $\delta^{13}C$ and $^{13}CH^-/^{13}C^-$ ratios. Only two of our $^{13}C^-$ count rate values are higher than 6×10^5 counts per second, and most of our data are in the range of $2–5 \times 10^5$ counts per second (Supplementary Table 1). The measured deadtime of the EM detector was 23 ± 2 ns and no correlation (beyond the analytical uncertainty) is observed between $\delta^{13}C$ and the count rate on ^{12}C for standard analyses or within each bracketed set of unknowns.

3.5. Assessing matrix-effect bias in SIMS

Isotopic biases may arise in SIMS data due to a number of sample-specific factors including isobaric interferences, isotopic fractionations created by breaking of different bonds such as C–H, C–C, C=C, and mixtures in variable proportions of elements of interest and matrix constituents (Riciputi and Greenwood, 1998; Sangély et al., 2005). Such factors may influence the measure of $\delta^{13}C_{org}$ and $^{13}CH^-/^{13}C^-$. Fig. S5A and B and the Supplementary Table 1 show that no significant relation exists between the ^{12}C count rate and the distinctive $\delta^{13}C$ values recorded for each OM texture type (Figs. 1–4) in all our samples. Thus, we have not applied a correction on $\delta^{13}C_{org}$ for matrix effect arising from variable ratio of sputtered OM to sputtered quartz matrix. This is in good agreement with previous SIMS $\delta^{13}C$ studies of OM-silicate (Sangély et al., 2005) and carbonate-sulfide-oxide mixtures (Riciputi and Greenwood, 1998). One SIMS pit revealed K-rich phyllosilicates (likely muscovite) within micro-veins (Fig. S10B). This spot and another one in this phyllosilicate-rich vein show a $\delta^{13}C_{org}$ value that is ~2‰ higher than other spots in this vein and in a phyllosilicate-free vein (Figs. 2, S9 and S10). Spots in the phyllosilicate-rich vein do not show a higher $^{13}CH^-/^{13}C^-$ signal, hence there is no evidence that phyllosilicate hydrogen has recombined in the SIMS

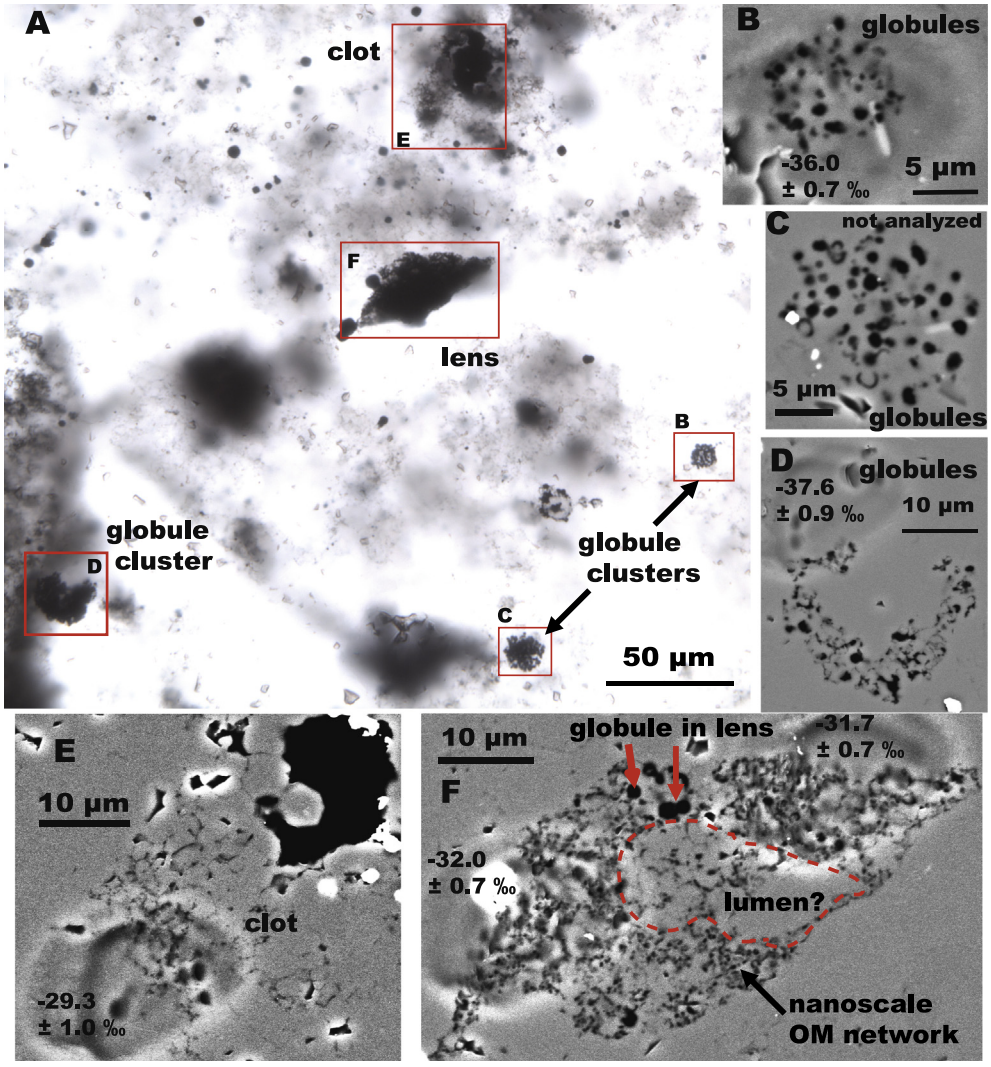

Fig. 1. Various, closely associated OM microstructures in sample WF4. (A) Photomicrograph of region D7. (B–F) BSE images of regions marked in A showing SIMS pits and associated values of $\delta^{13}C$ with analytical uncertainty. The chert is composed of quartz (gray) and OM (black). (B–D) Globule clusters. (E) Clot. (F) Lens mostly composed of a dense network of nanoscale OM and a few globules (arrows). Density of the OM network is lower in the outlined area. The upper SIMS pit intercepted several globules.

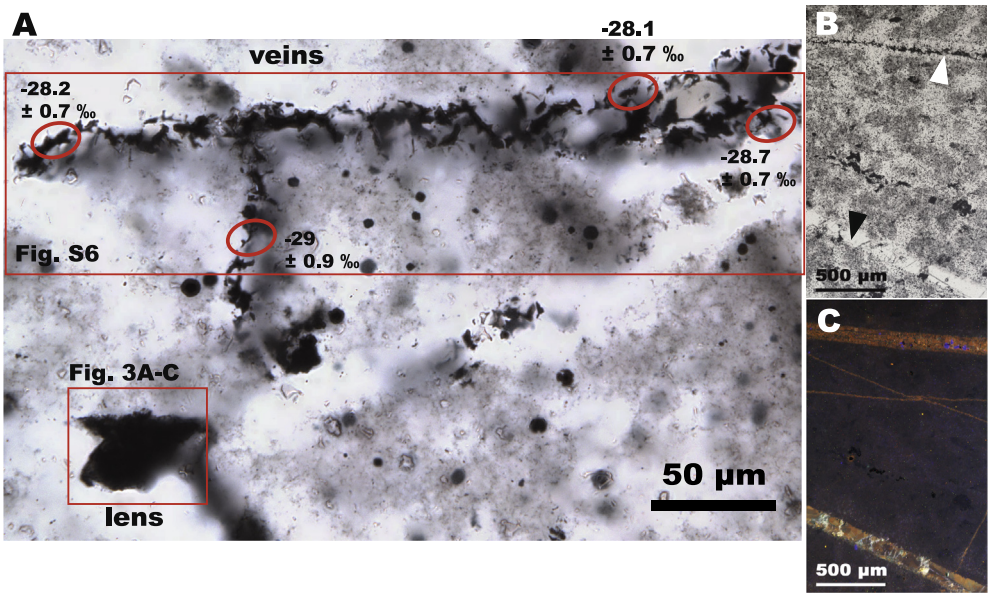

Fig. 2. OM-rich quartz micro-veins in sample WF4. (A) Multiplane (here two focal planes) combination of photomicrographs of region B1(v1,sp) showing a lens and a lens fragment (lower box) in a region cut by numerous pure quartz and OM-bearing quartz micro-veins. Ellipses highlight SIMS analysis spots with associated $\delta^{13}C_{org}$ (‰ VPDB) values and analytical uncertainty. (B) Transmitted light photomicrograph showing OM-rich (white arrow) and ZnS-rich (black arrow) quartz micro-veins. (C) Cathodoluminescence image of the same region. Quartz micro-veins appear orange, ZnS is light green. (For interpretation of the references to color in this figure legend, the reader is referred to the online version of this article.)

plasma with $^{13}C^-$ ions and interfered on the $^{13}CH^-/^{13}C^-$ of OM (Fig. 5A). Because we cannot rule out a matrix effect on the three data points in the phyllosilicate-rich micro-vein, these data are excluded from the following.

Tests demonstrated that contamination from the quartz matrix and sample surface are negligible in our measurements of $^{13}CH^-/^{13}C^-$ and $\delta^{13}C_{org}$. First, any organic contaminants adsorbed onto sample surface are sputtered before analysis and the effect is negligible. Indeed, $^{13}CH^-$ count rate on OM-free quartz grains dropped below 20 cps within 10 s, which is between two and three orders of magnitude lower than $^{13}CH^-$ count rates recorded in zones with lowest $^{12}C^-$ count rates from OM (Supplementary Table 1). Second, at a mass resolution of 2200, $^{28}Si^{2-}$ (provided any is emitted) can be resolved and $^{12}CH_2^-$ appears as a shoulder on the $^{13}CH^-$ peak, but this shoulder only has 5% of the intensity of $^{13}CH^-$ ions and is thus neglected. Finally, hydrogen measured as $^{13}CH^-$ comes largely from OM in samples and not from $^{13}CH^-$ formed by recombination of $^{13}C^-$ sputtered from OM in samples with hydrogen from OH in quartz, or adsorbed onto sample surface. Indeed, there is no relation between $^{12}C^-$ count rate and $^{13}CH^-/^{13}C^-$ in the cherts (e.g. PPRG215-1, Fig. S5C): even at low $^{12}C^-$ count rates, where OM is less abundant and the volume of sputtered chert matrix is relatively high, $^{13}CH^-/^{13}C^-$ does not show significant increase from H addition. Hence, $^{13}CH^-/^{13}C^-$ is a good proxy for H/C.

The variable matrix effect caused by different H/C ratios between sample and standard has been shown as a possible source of bias in SIMS $\delta^{13}C_{org}$ analyses, especially for low maturity kerogen (Sangély et al., 2005; Williford et al., 2011b). However, the SPF OM has been metamorphosed in the sub-greenschist to lower greenschist facies. The PPRG215-1 standard (Fig Tree Group, Barberton, South Africa (Hayes et al., 1983; Walter et al., 1983; Tice et al., 2004) and our SPF OM show similar metamorphic grades (Sugitani et al., 2010). PPRG215-1 has a bulk rock H/C of 0.16 (Hayes et al., 1983), which is within the range of low H/C ratios measured in SPF cherts (Marshall et al., 2007). PPRG215-1 has a relatively narrow (range: 0.054–0.077, average: 0.064 ± 0.007, 1 standard deviation, Fig. S5C), almost normal $^{13}CH^-/^{13}C^-$ distribution, with the exception of one outlier at 0.032, arguing for OM homogeneity. WFL2-1 also shows a narrow range of $^{13}CH^-/^{13}C^-$ (0.033–0.040), but a much lower average $^{13}CH^-/^{13}C^-$ of 0.036 ± 0.002 (1SD). The texturally homogenous OM (Fig. S2) in WFL2-1 shows homogeneous $\delta^{13}C_{org}$ values averaging -27.1 ± 0.73‰ VPDB (1SD, $n = 13$), close to the bulk kerogen value of -27.4‰. This result strongly argues that our $\delta^{13}C_{org}$ measurements are accurate and that the $^{13}CH^-/^{13}C^-$differences between WFL2-1 and PPRG215-1 are corrected within precision by the techniques described here. The average $^{13}CH^-/^{13}C^-$ of two other SPF cherts is closer to that of PPRG215-1: 0.067 ± 0.014 (1SD) for WF4 and 0.074 ± 0.009 (1SD) for PAN1-1A, but $^{13}CH^-/^{13}C^-$ ranges are wide (Fig. 5: 0.038–0.108 for WF4; 0.055–0.092 for PAN1-1A). These two samples show a weak positive relationship between $\delta^{13}C_{org}$ and $^{13}CH^-/^{13}C^-$ (Fig. 5; $R^2 = 0.23$ for WF4 and 0.24 for PAN1-1A). In contrast, instrumental bias caused by kerogen with different H/C ratios produces a negative correlation (Sangély et al., 2005; Williford et al., 2011b). In our samples, the weak positive relation can only be explained by true $\delta^{13}C_{org}$ and H/C heterogeneities.

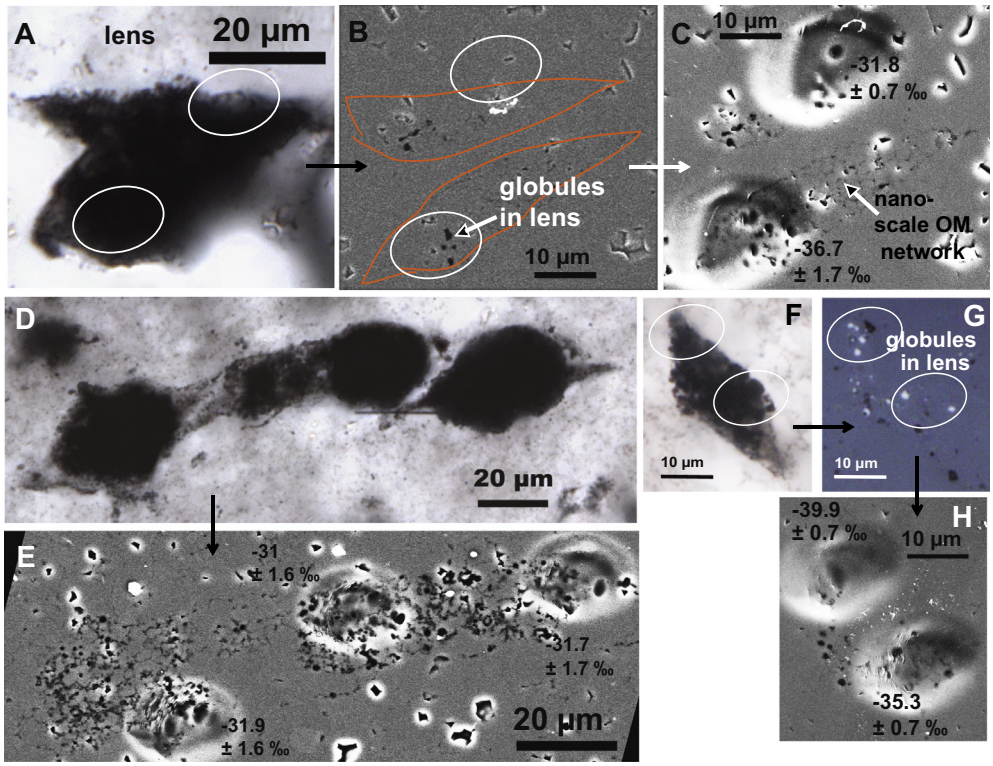

Fig. 3. Textures of lenses in sample WF4. (A) Multiplane photomicrograph of two lenses in region B1(v1,sp) as shown in Fig. 2. The upper lens is cut by a chert vein. (B) SE image of the same region. Ellipses highlight SIMS targets. Orange lines highlight parts of the two lenses that intersect the surface of the thin section. The lower target displays OM globules, whereas the upper one does not. (C) BSE image of the same region showing SIMS pits with associated $\delta^{13}C_{org}$ (‰ VPDB) data, and the network of nanoscale OM in lenses. (D) Multiplane photomicrographs of region D4 showing three linked lenses. The black linear feature at the center right is a sulfide crystal. (E) BSE image of the same region. These lenses are mostly composed of a network of nanoscale OM and only include a few globules. Obvious globules (SE image not shown) were only intercepted in the lower right SIMS spot. (F–H) Region D3sp2 showing a globular lens. (F) Transmitted light photomicrograph, (G) reflected light photomicrograph, and (H) BSE of the same region. (For interpretation of the references to color in this figure legend, the reader is referred to the web version of this article.)

Individually, OM-texture types do not show relations between $\delta^{13}C_{org}$ and $^{13}CH^-/^{13}C^-$. Linear relations link CN^-/C^- to atomic N/C (van Zuilen et al., 2007) and $^{13}CH^-/^{13}C^-$ to H/C (Williford et al., 2011b) in a compositional series of pure OM standards. We did not produce such a calibration line. However, using the bulk kerogen H/C value (0.16 at%, Hayes et al., 1983) and the average SIMS $^{13}CH^-/^{13}C^-$ (0.064) of our PPRG215-1 standard, we can infer that the atomic H/C value recorded in our samples (maximum $^{13}CH^-/^{13}C^- = 0.108$ in WF4) is no higher than 0.27 ($=0.16 \times 0.108 \div 0.064$). This is within the range of H/C (0.02–0.46) measured by Marshall et al. (2007) in bulk SPF kerogen. Within the small range of H/C (<0.27) we measured, the effect of H/C on bias is <1‰ (House et al., 2000; Sangély et al., 2005; Williford et al., 2011b, 2013) and cannot explain the range of $\delta^{13}C_{org}$ compositions analyzed from SPF-OM.

4. OM TEXTURES

The stromatolitic chert WFL2-1 shows a homogenous texture composed of diffuse, globular masses of OM nanoparticles (Fig. S2). The WF4 and PAN1-1A cherts show clusters of cell-like lenses ca. 20–70 µm in length (Figs. 1–3, S11, S14–16, S19 and S20) and clusters of cell-like spheres ca. 10 µm in diameter (Figs. 4, S12, S17). Spheres and lenses are impregnated by chert. Similar to the Farrel Quartzite lenses (Oehler et al., 2010), the SPF lenses are lenticular to spheroidal bodies displaying a flange-like appendage (Sugitani et al., 2010, 2013), and they comprise a reticulate nanoscale organic network interspersed with variable amounts of micrometer-scale pure OM globules (Figs. 1F, and 3). Three types of internal textures were identified within lenses: (i) lens type 1 that does not show globules, (ii) lens type 2 that displays OM particles larger than the rest of the nanoscale reticulate OM that either represent small globular inclusions or larger non-globular reticulate OM at grain boundaries, and (iii) lens type 3 that displays ~1 µm large rounded globules. All types of lenses commonly display OM-free lumens (Figs. S11, S14, S19) or zones where the reticulate OM network is less dense (Fig. 1F). Spheres consist of an organic wall thinner than a micrometer that pinches and swells, but do not show internal globular OM as lenses do (Fig. 4). WF4 and PAN1-1A also show clusters of rounded, ~1 µm diameter pure-OM globules (Figs. 1B–D, 4C, and S18) as well as dense clots composed of nanoscale to microgranular OM distributed along the grain boundaries of micro-quartz (Figs. 1E, S10D, S13, S21, and S22).

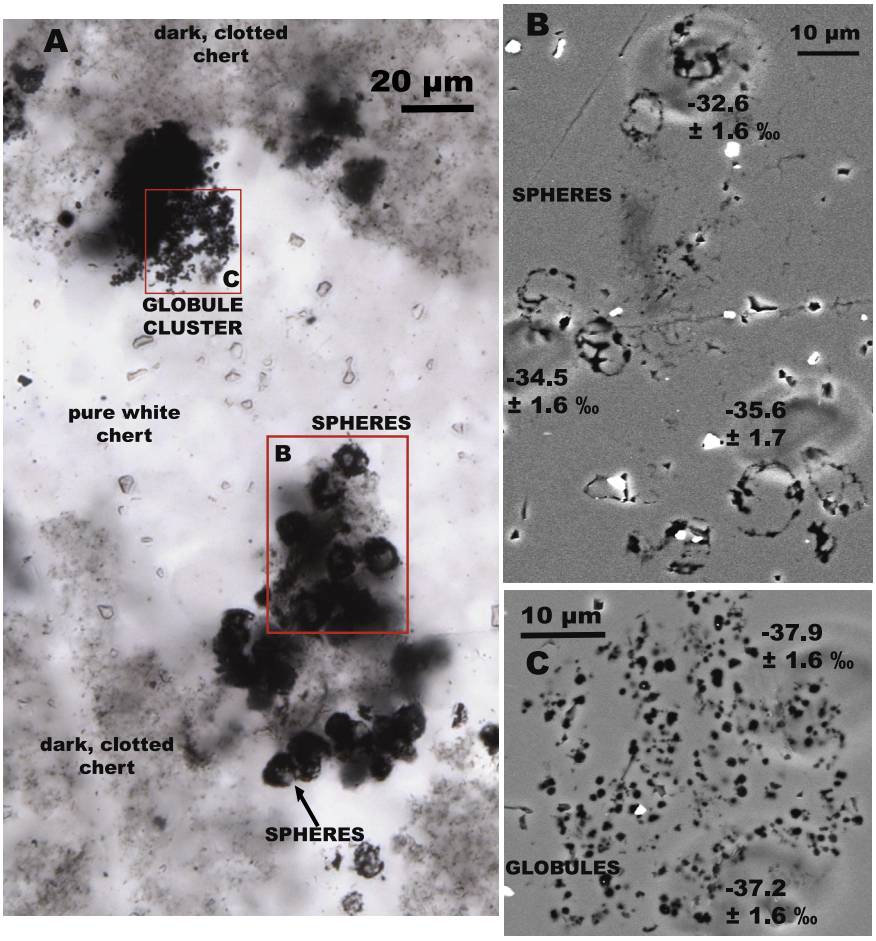

Fig. 4. Clusters of spheres and globules in sample WF4. (A) Photomicrograph of region D8-s2. (B and C) BSE images of regions marked in A showing SIMS pits and associated carbon isotope data with analytical uncertainty as defined in Supplementary Eq. (3). (B) Cluster of spheres. (C) Globule cluster.

In WF4 and PAN1-1A, the chert matrix either shows diffuse nanoscale OM distributed at grain boundaries in a dark clotted fabric, or is composed of pure white chert (Figs. 4A, S3, S4, and S11). The latter does not show a distinct color in cathodoluminescence (Fig. 2B and C) or a distinct quartz crystal size under crossed polarization. Micro-veins filled by OM particles (commonly larger than 10 µm; Fig. 2) occur only in WF4 and cut across both white and dark clotted chert fabrics. Spheres, lenses, clots and globules are widespread and do not show any spatial relationship with the OM-bearing micro-veins (Sugitani et al., 2010 and Figs. S9–S22). When observed optically by cathodoluminescence, silica in micro-veins luminesces orange, whereas the matrix chert does not luminesce (Fig. 2B and C). Thus, the late vein-filling silica shows distinct trace element composition compared to the relatively homogenous chert matrix hosting spheres, lenses, clots and globules.

5. SIMS ANALYSES: H/C–δ^{13}C HETEROGENEITIES

For each OM-texture type, we show the relations between $^{13}CH^-/^{13}C^-$ and $\delta^{13}C$ (Fig. 5), the $\delta^{13}C$ distributions (Fig. 6), and the $\delta^{13}C$ and $^{13}CH^-/^{13}C^-$ ranges (Table S2). The stromatolitic chert WFL2-1 shows homogeneous texture, $^{13}CH^-/^{13}C^-$ (average 0.036) and SIMS $\delta^{13}C_{org}$ similar to bulk values (−27.4‰ VPDB). The massive chert WF4 shows an 11.8‰ range of SIMS $\delta^{13}C_{org}$ values (−39.9‰ to −28.1‰ VPDB) in agreement with the bulk value [−31.01‰ (Sugitani et al., 2010)]. Type-1 lenses, spheres, and globules in WF4 show approximately normal $\delta^{13}C_{org}$ distributions that exhibit only minor overlap and are distinct from the $\delta^{13}C_{org}$ of micro-veins (Figs. 6, S9–S16). OM in phyllosilicate-free micro-veins is highest in $\delta^{13}C$ (−29.0‰ to −28.1‰, average −28.5‰). Micro-veins show the widest range of $^{13}CH^-/^{13}C^-$ (0.068–0.108) and the highest maximum and average (0.085) values. In sharp contrast, globules show the lowest $\delta^{13}C_{org}$ (average −37.4‰), and a narrow range of low $^{13}CH^-/^{13}C^-$ values (0.053–0.058). The distribution of $\delta^{13}C_{org}$ in spheres shows a sharp peak between −35‰ and −36‰, little overlap with the more negative globules, and a tail at higher values (Fig. 6B). Values of $^{13}CH^-/^{13}C^-$ in spheres are on average low (0.054) and close to globules, though a wider range is observed (0.044–0.07). Lens types 1–3 were analyzed in WF4. Type 1 lenses (without globules) and type 2 (possible globules)

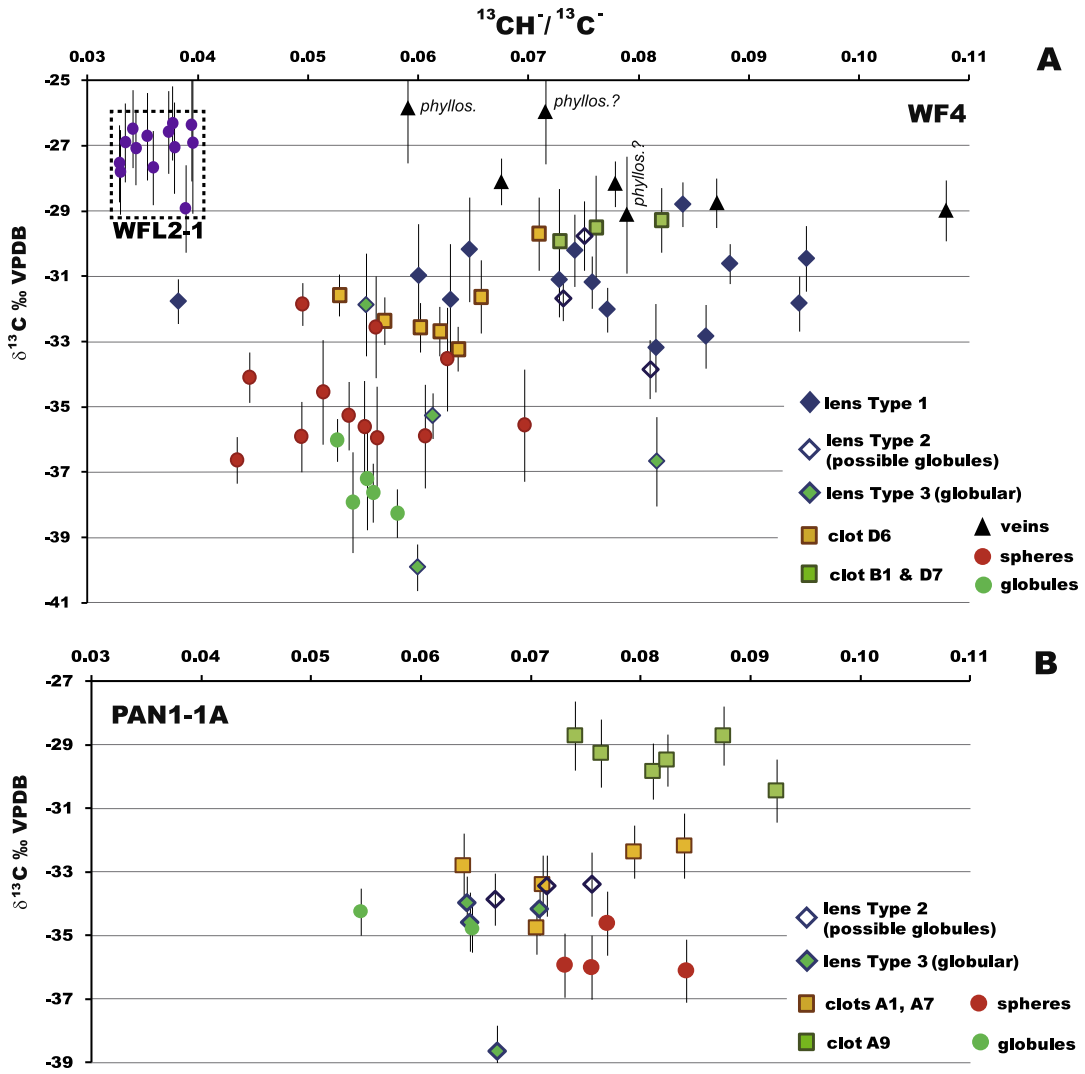

Fig. 5. $\delta^{13}C$ (‰ VPDB) SIMS data as a function of $^{13}CH^-/^{13}C^-$ SIMS ratio. (A) samples WF4 and WFL2-1 (boxed) and (B) PAN1-1A. Error bars indicate analytical uncertainty as defined in Supplementary Eq. (3). For both panels: type-2 lenses with possible globules (open diamonds), type-3 globular lenses (green diamond), spheres (red filled circle), globules (green filled circle). For WF4 only: type-1 lenses where no globules were analyzed (blue diamond), veins (black triangles; "phyllos." indicates the analyses in the phyllosilicate-bearing vein), clots B1 and D7 (green square), clot D6 (orange square). For PAN1-1A only: clot A9 (green square), clot A1 and A7 (orange square). (For interpretation of the references to color in this figure legend, the reader is referred to the online version of this article.)

show a normal distribution with a peak between −30‰ and −32‰ and similar average values (−32.2‰ and −31.8‰, respectively). These two lens types show a wide range of $^{13}CH^-/^{13}C^-$ (0.038–0.095) with an average at 0.075. Type-3 lenses (globular) have lower $\delta^{13}C_{org}$ (average −35.9‰) and lower average $^{13}CH^-/^{13}C^-$ (0.065) and values are close to those of globule clusters. Most globules in clusters, and type-3 globular lenses, show a higher $^{12}C^-$ count rate than other lenses (Fig. S5). Micrometer-scale globules in type-3 lenses thus represent a major contribution to the SIMS carbon signal compared to the surrounding network of nanoscale OM matrix common in most lenses. Clots show $\delta^{13}C$ values limited to the range −33.2‰ to −29.3‰ with a bimodal distribution. The $\delta^{13}C_{org}$ of clot D6 (average −32‰) overlaps with that of lenses, whereas clots B1 and D7 show higher $\delta^{13}C_{org}$ (average −29.6‰) close to that of micro-veins. Both types of clot show a narrow range of $^{13}CH^-/^{13}C^-$ (D6: 0.053–0.071; B1–D7: 0.073–0.082), and clots with the highest $\delta^{13}C_{org}$ show the highest average $^{13}CH^-/^{13}C^-$ (B1–D7: 0.077), whereas the clot with lower $\delta^{13}C_{org}$ shows lower $^{13}CH^-/^{13}C^-$ (D6: 0.062).

In the laminated chert PAN1-1A, SIMS data show similar trends, although the smaller size of the dataset limits its statistical significance (Figs. 5B, 6F–I, S17–22). The range of SIMS $\delta^{13}C_{org}$ values (−38.6‰ to −28.7‰) is close to that observed in WF4, in agreement with the bulk $\delta^{13}C_{org}$ (−32.07‰). There are no micro-veins in PAN1-1A. Cell-like structures are less abundant than in WF4, and globule-free regions (lenses type 1) could not be targeted with certainty within lenses. Type-2 lenses show an average $\delta^{13}C_{org}$ of −33.6‰ (−33.9‰ to −33.4‰) and $^{13}CH^-/^{13}C^-$ of ca. 0.071 (0.067–0.076). Type-3 globular lenses show

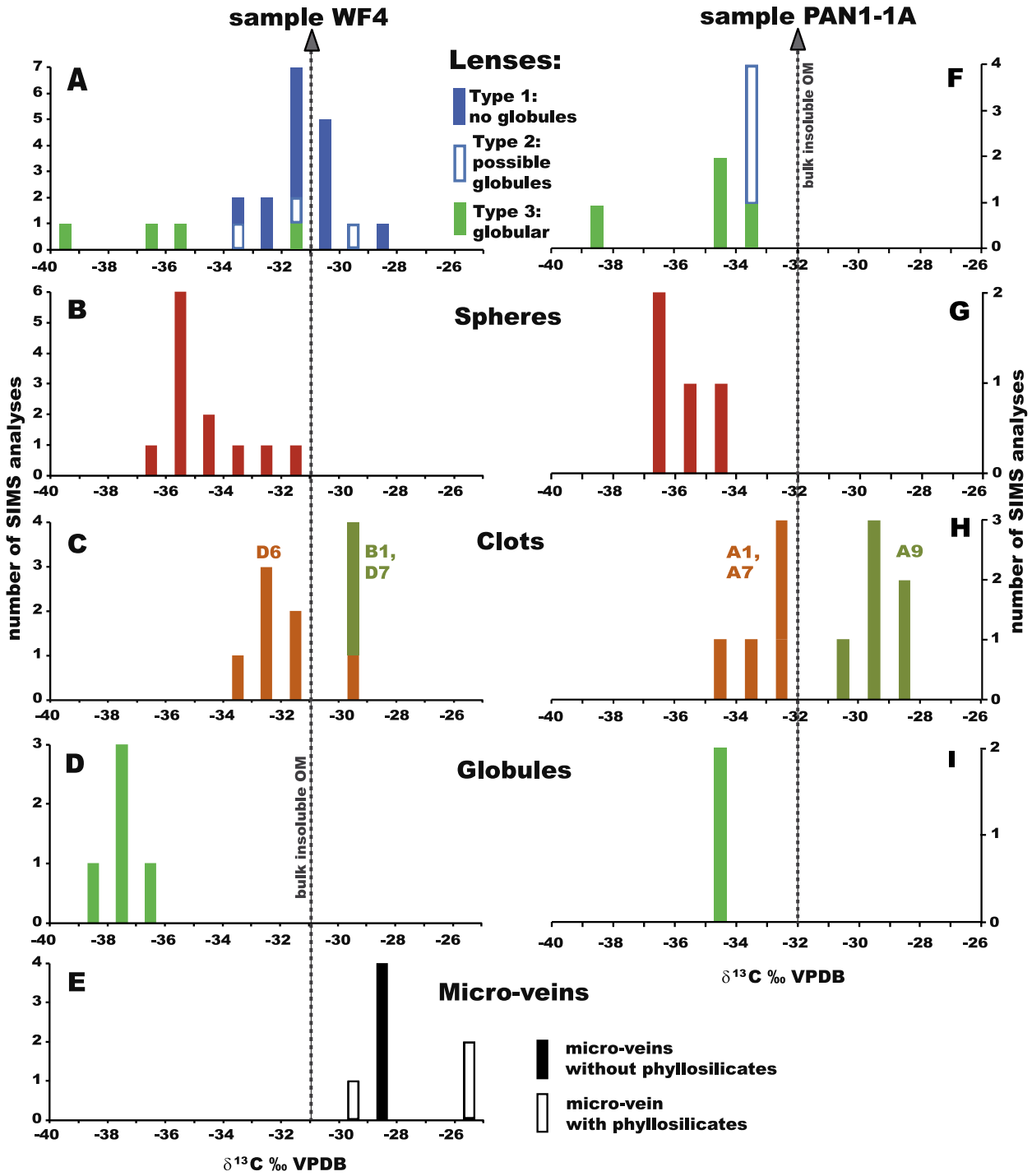

Fig. 6. Carbon isotope ratios of different OM-texture types in the Strelley Pool Formation cherts: histograms of SIMS data for each OM-texture type in sample WF4 (A–E), and sample PAN1-1A (F–I). Dashed lines indicate bulk analyses of $\delta^{13}C$ (‰ VPDB) for insoluble OM in each sample. In A and F, three types of internal textures are defined in lenses: type-1 lenses where no OM globules were observed in the OM network (blue, centered on the mean), type-2 lenses with few, small, or possible globules (outlined), and type-3 globular lenses (green). (B and G) Spheres. (C–H) Clots. In C, analyses in orange are from clot D6, and analyses in green are from clots B1 and D7. In H analyses in orange are from clot A1 and A7, and analyses in green from clot A9. (D and I) Globule clusters. In E, analyses in two types of micro-veins are distinguished: without phyllosilicates (black) and phyllosilicate-bearing micro-vein (outlined). (For interpretation of the references to color in this figure legend, the reader is referred to the online version of this article.)

lower $\delta^{13}C_{org}$ of ca. −35.3‰ (−38.6‰ to −34‰) and lower $^{13}CH^-/^{13}C^-$ of ca. 0.067 (0.064–0.071). As for WF4, these values are close to those in globule clusters, $\delta^{13}C_{org}$ (average −34.5‰) and $^{13}CH^-/^{13}C^-$ (0.055–0.065), although only two globule clusters were analyzed. The spheres in PAN1-1A also show a low $\delta^{13}C_{org}$ (average −35.7‰). Finally,

clots in PAN1-1A show a bimodal $\delta^{13}C_{org}$ distribution like that of WF4, with low $\delta^{13}C_{org}$ clots (A1, A7: average −33.1‰) displaying lower $^{13}CH^-/^{13}C^-$ (average 0.074), and high $\delta^{13}C_{org}$ clots (A9: −29.4‰) displaying roughly higher $^{13}CH^-/^{13}C^-$ (0.082).

6. RAMAN SPECTRA

All Raman spectra of OM (Fig. 7) display a small, flat D4 band near 1200 cm^{-1} and a poorly developed D3 band near 1500 cm^{-1}. All spectra present a D1 band near 1345 cm^{-1} with an intensity that varies relative to that of a G + D2 doublet of maximum intensity near 1600 cm^{-1}. In WFL2-1 and most WF4 OM-texture types, the D2 band appears as a well-resolved shoulder at ca. 1612 cm^{-1}. In contrast, OM micro-veins in WF4, and all textures types in PAN1-1A show a symmetric G + D2 doublet where the D2 band is not resolved. However, the G + D2 center is not significantly shifted toward the G-band position at 1580 cm^{-1}. This implies that the contribution of the D2 band to the G + D2 doublet is relatively more important (Beyssac et al., 2002) in WF4 micro-veins and PAN1-1A compared to other WF4 textures, where the D2 band is only a shoulder flanking the G band. Finally, we have analyzed the same OM grains at the polished surface and their extension below the surface of quartz grains. Polished OM shows increased G + D2, D3 and D4 bands compared to pristine OM, which is consistent with increased disorder artifacts associated with polishing (Beyssac et al., 2003). As a quantitative structural parameter, we have measured the ratio of the height of the D1 band to that of the G + D2 doublet (Table 1). WFL2-1 displays the highest D1/(G + D2) ratio of 1.58. Within one standard deviation, clots, globules, lenses and spheres in WF4 show similar D1/(G + D2) ratios of ca. 1.48 (average). Veins in WF4 show a distinct ratio of ca. 1.24. In PAN1-1A, lenses, spheres and globules show a similar D1/(G + D2) ratio of ca. 1.10. Clots in PAN1-1A show a slightly lower average D1/(G + D2) ratio of ca. 1.01, although the range of values largely overlaps with those in other OM-texture types. The variability in each OM-texture type may be explained by analysis of polished OM nanoparticles while targeting OM grains deep within thin sections.

Table 1
Height ratios of the Raman bands: D1/(G + D2).

WF4	Lenses	Spheres	Globules	Clots	Veins
Mean	1.47	1.51	1.44	1.47	1.24
Std. Dev.	±0.07	±0.12	±0.11	±0.06	±0.09
n	17	14	10	18	20
Min.	1.37	1.32	1.32	1.35	1.05
Max.	1.62	1.70	1.59	1.56	1.40
PAN1-1A	Lenses	Spheres	Globules	Clots	
Mean	1.10	1.09	1.12	1.01	
Std. Dev.	±0.06	±0.04	±0.03	±0.06	
n	8	5	5	13	
Min.	1.03	1.04	1.09	0.90	
Max.	1.19	1.14	1.16	1.13	
WFL2-1 (globular clots)				1.58	±0.02

7. DISCUSSION

Metamorphic alteration of primary OM and addition of migrated OM may have altered the $\delta^{13}C_{org}$ and generated secondary heterogeneities. Earlier in the history of the host rocks, diagenetic processes and putative hydrothermal organic synthesis may have obscured the isotope signal of the primary biogenic micro-reservoirs. OM petrography, and in situ $\delta^{13}C_{org}$ and H/C analyses, coupled with an assessment of structural order in OM using Raman microspectrometry provide novel insights into these processes. We will discuss in a sequential order: (1) the effects of metamorphic alteration, (2) possible migrations post-dating peak metamorphism, (3) arguments showing that all OM micro-reservoirs except micro-veins pre-date peak metamorphism, (4) possible pre-metamorphic migrations, and (5) metabolic, biosyn-

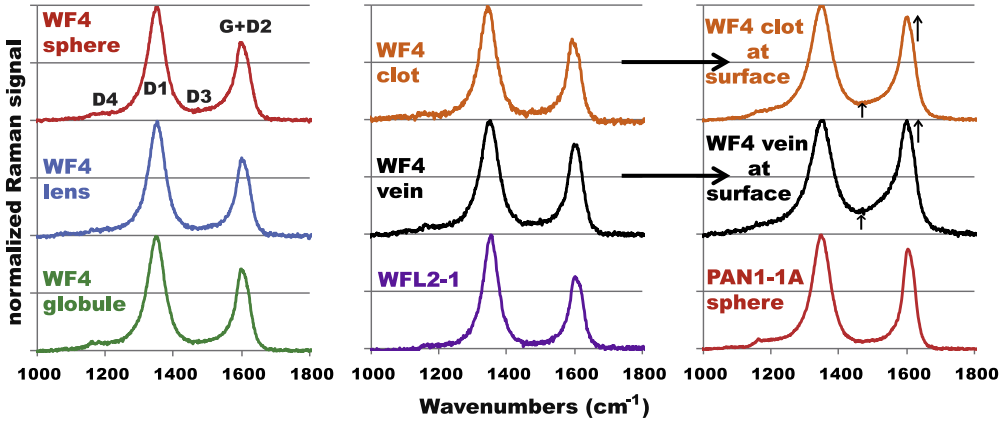

Fig. 7. Representative Raman spectra of OM in samples WF4, PAN1-1A, and WFL2-1. The two upper spectra in the right section were recorded on polished OM intersecting the surface of thin sections. All other spectra were recorded on unpolished OM occurring below the surface under quartz grains. Arrows highlight the changes in Raman spectra caused by artefacts occurring in polished OM, compared to the same unpolished OM as discussed in the main text.

thetic, diagenetic and hydrothermal processes forming primary $\delta^{13}C_{org}$ and H/C heterogeneities.

7.1. Metamorphic alteration of OM

During thermal maturation, the first order Raman spectrum of OM evolves until carbon reaches the structure characterized by a single G-band characteristic of triperiodic graphite at 1580 cm^{-1} (Beyssac et al., 2002). Other bands, characteristic of disorder in the pre-graphitic structures, usually show the following evolution with increasing metamorphism. Low-grade OM usually shows a broad D1 + D4 band that is small compared to the G + D2 band at temperatures lower than 300 °C (Lahfid et al., 2010). The height of the D1 band increases relative to that of G + D2 with increasing metamorphism, whereas D3 and D4 decrease. For WF4 OM-texture types other than veins, we measured a R2 band area ratio (D1/(D1 + G + D2) of 0.68 (Sugitani et al., 2010), which suggests a peak metamorphic temperature of ca. 340 °C (Beyssac et al., 2002). This temperature lies at the lower limit of the Raman geothermometer proposed by Beyssac et al. (2002). At such low metamorphic grades, heterogeneous organic precursors (Lahfid et al., 2010), time, fluid composition, and mineral matrix (Hetenyi, 1995) may affect maturation and structural ordering of OM. The accuracy of the geothermometer of Beyssac et al. (2002) inferred from OM in metapelites may be limited in rocks of different mineralogy such as the cherts studied here. Therefore, we will use the term "structural order" rather than "metamorphic grade". Above about 300 °C, the relative intensity of the D2 relative to the G band decreases: the G + D2 doublet becomes resolved and asymmetric (Lahfid et al., 2010). It is only at higher degrees of structural order that the D1 band decreases in relative height until almost complete disappearance, and at these degrees of order, D2 would only appear as a small shoulder (Beyssac et al., 2002). Hence, the absence of a resolved D2 shoulder in the G + D2 doublet centered at ca. 1600 cm^{-1} in veins of WF4 and in sample PAN1-1A (Fig. 7) implies that these OM components show a lower degree of structural order compared to other OM-texture types in WF4. Assuming precursor effects are negligible, using temperature-calibrated spectra from contact metamorphic localities (Lahfid et al., 2010), it can be inferred that (1) the OM in WF4 micro-veins is slightly less mature than that in other textures, and (2) OM in PAN1-1A chert is likely less mature than OM in WF4. Conversely, the more pronounced D2 shoulder and the slightly higher relative height of D1 implies a slightly higher degree of structural order in WFL2-1 compared to WF4. Thus, the structural order attained by OM in our samples is inversely proportional to our D1/(G + D2) height ratio (Table 1). The best-preserved OM analyzed in this study occurs in PAN1-1A and is likely less metamorphosed compared to WF samples that come from a distinct greenstone belt. The structural order heterogeneities observed between veins and other OM-texture types in WF4, and WFL2-1 located only 50 m away from WF4 cannot be explained by regional scale variations in metamorphism. A number of factors may contribute to these heterogeneities: (1) mineral matrix effects (van Zuilen et al., 2012), (2) polarization of the Raman signal by oriented arrangement of graphitic/polyaromatic domains (Beyssac et al., 2003), (3) differential alteration during metasomatism linked with fluid pathways (Allwood et al., 2006b), (4) organic precursor effects (Quirico et al., 2009; Bernard et al., 2010b), and (5) OM migration during/between different stages of the metamorphic history of the SPF. These factors are evaluated below.

First, the mineral matrix of analyzed OM is always quartz. Thus, mineral matrix templating is unlikely to be responsible for the structural order heterogeneities observed in our samples. Second, recent analyses of carbonaceous matter of higher structural order than the SPC OM in different orientations with respect to the incident laser have shown that polarization effects by graphic lattice are unimportant (Aoya et al., 2010), and can therefore be ruled out in the SPF OM. Third, alteration of organic matter during metamorphism typically increases bulk $\delta^{13}C_{org}$ values, because of alteration reactions with preferential loss of low-$\delta^{13}C$ CH_4 (Des Marais, 2001; Ueno et al., 2004), and because of isotopic exchange between OM and inorganic C, principally carbonate minerals (Valley, 2001; van Zuilen et al., 2007; Pinti et al., 2009a). This $\delta^{13}C_{org}$ increase is systematically correlated (Fig. 8A) with decreasing H/C and N/C (Des Marais, 2001; Ueno et al., 2004; van Zuilen et al., 2007). However, in WF4 and PAN1-1A, H/C shows a weak positive correlation with $\delta^{13}C_{org}$ (Fig. 8A). Although the ranges of H/C are wide for different types of OM textures, there is a clear difference between globules and high-$\delta^{13}C_{org}$ clots (Fig. 6: B1, D7 in WF4, and A9 in PAN1-1A). Moreover, within the range of H/C observed in our samples (<0.27), $\delta^{13}C_{org}$ is only known to increase by 1–3‰ relative to the precursor (Des Marais, 2001; van Zuilen et al., 2007), which cannot explain the range of $\delta^{13}C_{org}$ values observed in SPF cherts. No carbonates were observed in thin sections of WF4 and WFL2-1. Isotopic equilibration between OM and carbonates is unlikely in these samples. Small, scattered rhombs of carbonate, likely dolomite or ankerite are scattered throughout PAN1-1A. Microscopic image analysis provides a crude estimation of the volume fraction occupied by carbonate (~1–16%) suggesting that PAN1-1A contains at least an order of magnitude more carbonate carbon (~0.14–2.3 wt%) than organic carbon (0.043 wt%, Supplementary methods). Furthermore, studies have shown that OM-carbonate isotope exchange is limited at low metamorphic grade and in such carbonate-poor rocks (Valley, 2001). The absence of a large bulk $\delta^{13}C_{org}$ difference between WF4 (carbonate-free) and PAN1-1A (carbonate-poor) supports the absence of substantial isotopic exchange in PAN1-1A. Moreover, PAN1-1A carbonates are not specifically associated with any of the OM-texture types; hence isotopic exchange could only have affected all OM-texture types equally.

Altogether, our data rule out the possibility that $\delta^{13}C_{org}$ and H/C heterogeneities in WF4 and PAN1-1A were formed from a single precursor by heterogeneous metasomatism at sub-millimeter scales. Primary organic precursor effects and/or migration of OM are thus required to explain the Raman, $\delta^{13}C_{org}$ and H/C heterogeneities in WF4 and

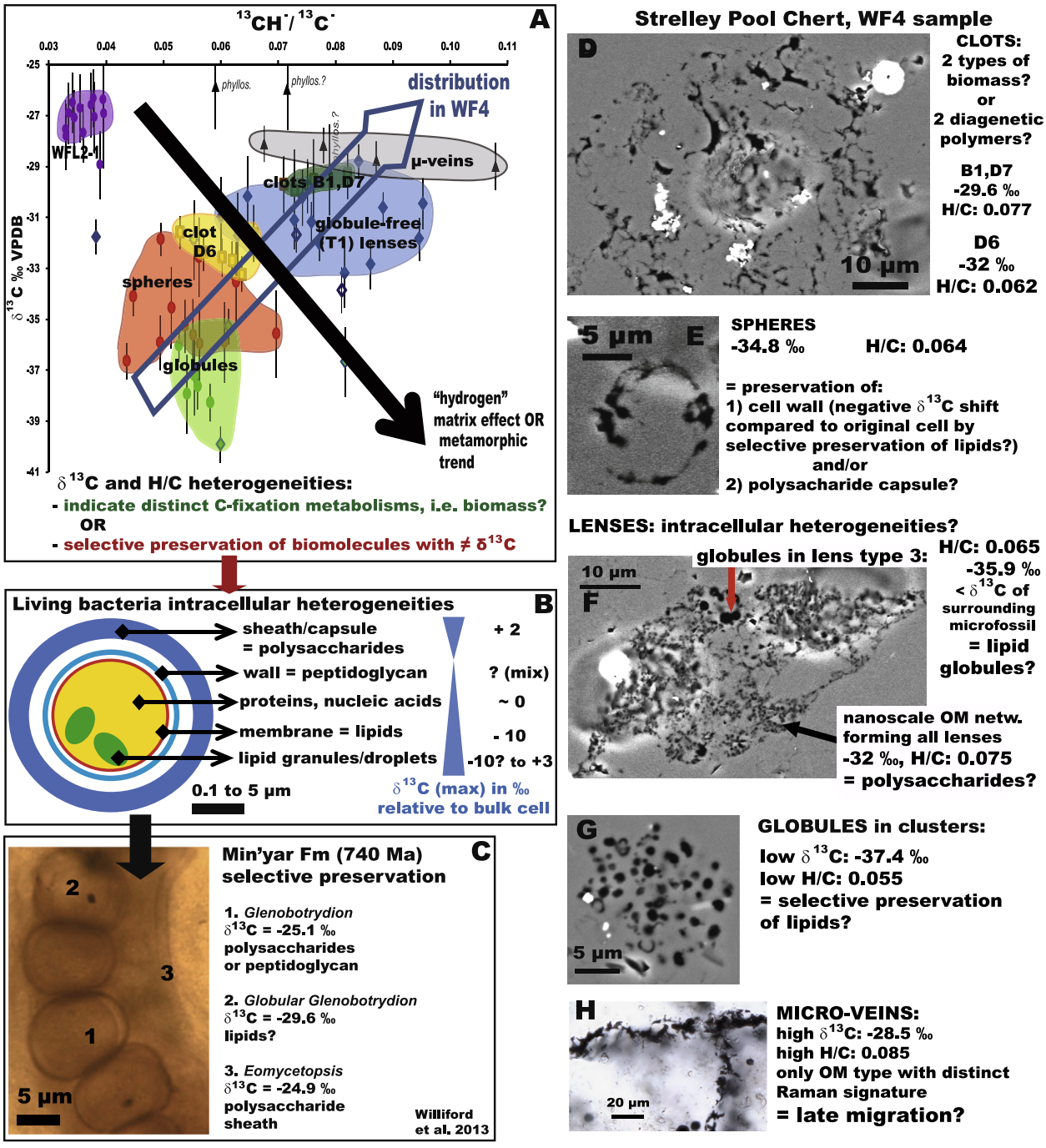

Fig. 8. Synthesis of the data and interpretations. (A) δ^{13}C *versus* $^{13}CH^-/^{13}C^-$ data from sample WF4 and WFL2-1. Values distinguishing different types of organic matter have been highlighted (a maximum one outlier is located outside of each highlighted regions of the diagram for each OM type). The general positive trend recorded in WF4 opposes that expected from matrix effects caused by variable hydrogen concentration in OM, and metamorphism, indicating that the heterogeneities observed in our samples are real and predate metamorphism. These heterogeneities can be explained either by different carbon-fixation metabolisms (e.g. photosynthesis *versus* methanogenesis), or by selective preservation of the distinct isotopic fractionations inherited from different precursor biomolecules. (B) In a single cell, different biomolecules form by distinct biosynthetic pathways that can impart molecule-selective isotopic fractionations. (C) SIMS studies have shown that intracellular isotopic heterogeneities can be preserved in ancient microfossils. Some 740 Ma old *Glenobotrydion* cells preserve internal globules with a δ^{13}C lower than that of the surrounding cell. Accordingly, these globules may have formed from a lipid-rich precursor (Williford et al., 2013). (D–H) Images of the different types of OM observed in sample WF4, associated with average δ^{13}C and $^{13}CH^-/^{13}C^-$ values, and interpretation of their organic precursor are based on coupled textural and isotopic criteria compared with B and C.

PAN1-1A. A global upwards shift of 1–3‰ with respect to precursor $\delta^{13}C_{org}$ during metamorphism is considered for all interpretations in the following discussion.

7.2. Late migrations in WF4

Compared to other OM-texture types, OM that migrated in micro-veins displays distinct Raman spectra and a higher H/C that are both indicative of less altered OM. Micro-vein OM may either represent indigenous or exogenous pyrobitumen. Proterozoic bitumen is usually higher in $\delta^{13}C_{org}$ than associated kerogen, which may be the result of the selective preservation of lipids from heterotrophic, rather than primary production biomass (Close et al., 2011). The higher $\delta^{13}C_{org}$ observed in micro-veins compared to other OM textures is thus consistent with an indigenous origin. In this model, the lower structural order measured by Raman in micro-vein OM can only be explained by a precursor effect as in situ bitumen would have formed earlier than peak metamorphism, which was intense enough to pyrolyze kerogen and bitumen. Thus far, however, precursor effects have not been demonstrated in rocks of sub-greenschist to lower greenschist facies. The fact that globules and high-$\delta^{13}C_{org}$ clots (B1, D7) show clearly distinct H/C (Fig. 8A) but a similar structural order (Fig. 7) suggests that different precursor compositions had no influence on OM structure. Conversely, the higher $\delta^{13}C_{org}$ could reflect the different composition of exogenous bitumen. Interestingly, in a rock submitted to burial and contact metamorphism up to the sub-greenschist to lower greenschist facies, kerogen and adjacent pyrobitumen showed distinct Raman spectra and lower structural order in pyrobitumen (Jehlička et al., 2003). The authors interpreted this structural difference as the result of different metamorphic regimes, requiring that kerogen was altered during burial metamorphism, and migrated pyrobitumen altered by subsequent contact metamorphism. Similarly, WF4 micro-veins may represent exogenous pyrobitumen altered by hydrothermal activity or a late regional metamorphic event less intense than earlier, peak metamorphism. In conclusion, OM in WF4 micro-veins represents pyrobitumen that migrated beyond the millimeter scale. Assuming that precursor controls on structure are unlikely in rocks of sub-greenschist to lower greenschist facies, an exogenous source post-dating peak metamorphism is most likely for micro-vein pyrobitumen.

7.3. OM predating peak metamorphism

7.3.1. Microstructures in WF4 and PAN1-1A

The similar Raman spectra of lenses, spheres, and globules in WF4 (Fig. 7) and PAN1-1A [Fig. 7 and (Sugitani et al., 2013)] argue against an origin post-dating peak metamorphism and are consistent with an indigenous source for all these structures. In WF4, all the dense clots also show a similar Raman spectrum. In WF4, Sugitani et al. (2010) analyzed one texturally distinct, spherical clotted texture composed of a myriad of micro- to nano-particles of OM rather than grain boundary coatings. One Raman analysis of this clot revealed a D1/(G + D2) ratio of 1.5 similar to the clots in the present study, as well as two other spots with D1/(G + D2) ratios of 1.9 and 1.25. The higher structural order particle (ratio of 1.9) may be explained by the presence of rare, transported material consistent with the well-rounded texture and diffuse OM microstructure distinct from all other clots analyzed in the present study. The particle with D1/(G + D2) of 1.25 is similar to vein OM in WF4, but may also represent a polishing artefact (Fig. 7). All Raman analyses were performed below sample surfaces in the present study. However, in the one clot analyzed by Sugitani et al. (2010), OM particles are extremely diffuse and analysis of polished surface material could not be ruled out. In PAN1-1A, clots on the average show a slightly lower structural order (Table 1) than other OM-texture types. Taken separately, both low (A1, A7) and high (A9) $\delta^{13}C_{org}$ clots in PAN1-1A show heterogeneities in OM structure: the D1/(D1 + G + D2) ratio ranges between 0.93 and 1.13 in clot A1 and between 0.9 and 1.05 in A9. As discussed above, it is difficult to assess whether such small structural heterogeneities represent a minor analytical artefact, a late migration, an orientation or a precursor effect. In conclusion, in WF4, all the clots with a similar grain-boundary network texture, as well as spheres, lenses and globules show a similar Raman spectrum indicative of peak metamorphism. The same is observed in PAN1-1A, although clots show more variability.

7.3.2. Stromatolitic OM in WFL2-1

In WFL2-1, $\delta^{13}C_{org}$ values are only slightly higher than those of micro-veins occurring in sample WF4 from the same outcrop. However, Raman spectra indicating higher structural order and the lower H/C imply that WFL2-1 OM is more altered than OM in WF4 micro-veins. Hence, WFL2-1 OM cannot represent the same pyrobitumen as that located in WF4 micro-veins. The possibility that WFL2-1 OM represents the precursor kerogen to the WF4-micro-vein pyrobitumen is unlikely. First, the high structural order in WFL2-1 indicates that it was metamorphosed during peak metamorphism. Second, the $\delta^{13}C_{org}$ of the parent kerogen is expected to be lower than that of bitumen (Close et al., 2011), and we observed the reverse situation. Thus, WFL2-1 OM is likely unrelated to WF4 micro-vein OM.

WFL2-1 OM also shows a lower H/C and a slightly higher structural order than all other WF4 OM-texture types. Allwood et al. (2006b) proposed that OM structural order heterogeneities in different parts of the SPF stratigraphy correlate with distinct seafloor or sub-seafloor hydrothermal metasomatic regimes. Similarly, localized, enhanced fluid flow through the distinct stromatolitic matrix may have slightly increased structural order in WFL2-1 compared to WF4.

7.4. Early OM migrations?

Migration of OM before the peak of metamorphism cannot be ruled out solely based on structural similarity. Coupled textural and geochemical data provide further constraints on the origin of the different OM-texture types. Most notably, within dense clots, pure OM grains up to

~10 μm in size indicate OM migration, which may be explained by several processes. Polymerization of OM following degradation may have occurred from the earliest stages of diagenesis. Moreover, clotted textures may represent ripped-up microbial mats (Tice and Lowe, 2006). Displacement and compression of OM at grain boundaries could have formed dense OM grains within clots. Alternatively, bitumen formed by thermal cracking may have polymerized into clots. Such "pyrobitumen nodules" are known to form (i) by rapid maturation during hydrothermal silicification (Buick et al., 1998) or (ii) around radiogenic detrital grains, either through radiogenic immobilization of migrating hydrocarbons (Buick et al., 1998) or through synthesis of abiotic bitumen by catalytic hydrogenation of CO_2 (Sangély et al., 2007).

The texture and $\delta^{13}C$ values recorded in the SPF clots are not consistent with radiobitumen aggregates. First, neither textures indicating that OM accumulated around and as a replacement of radioactive grains (e.g. OM-rims, shrinkage cracks, filled nodules: Buick et al., 1998) nor remnants or pseudomorphs of either a potential radiogenic mineral or more stable sulfides were observed in the SPF clots. Second, large $\delta^{13}C_{org}$ heterogeneities indicative of radiogenic bitumen (Sangély et al., 2007) were not observed within single clots. Thus, we found no evidence that the SPF clots are radiogenic bitumen aggregates.

Dense pyrobitumen globules ~1–10 μm in diameter were observed in hydrothermally silicified Paleoarchean cherts (Buick et al., 1998), hence rapid hydrothermal maturation is a candidate for the formation of the dense, rounded SPF globules. Other, larger OM globules formed by hydrothermal alteration only migrated at the sub-millimeter scale and remained closely associated to source kerogen clots from which they were expelled (Buick et al., 1998). However, no spatial relation links the clusters of dense OM globules and the dense OM clots in the SPF cherts, arguing against formation of the globules by alteration of the clots. Furthermore, Buick et al. (1998) argued that rapid occlusion of pore spaces by hydrothermal silicification curtailed hydrocarbon migration to a few millimeters at shallow depths, thereby ruling out long-range, late migrations. Alternatively, globules may represent diagenetic textures pre-dating cracking and migration. Similar clusters of ~1 μm globules, polymerized by sulfurization during diagenesis, were observed in carbonate layers of 2.7 Ga stromatolite that were not hydrothermally altered (Lepot et al., 2008, 2009).

The cherts show a general dark, clotted chert fabric defined by diffuse nanoscale OM coating grain boundaries (Figs. 4A, S3–S4, S11) that likely formed by displacement and/or aggregation OM during crystallization of the primary mineral matrix. Within this clotted fabric, the dense clots that we analyzed by SIMS and Raman may represent knots where the OM network is denser (Figs. 1A and E). This OM-rich clotted fabric is interspersed with pure white chert (Figs. 4A, S3 and S4) that may fill initial pores. The absence of OM inclusions in white chert or aggregated at the interface between these two types of chert strongly argues against hydrocarbon migration beyond the millimeter-scale. With the exception of scattered, possibly hydrothermal or metamorphic dolomite/ankerite rhombohedra in PAN1-1A (Figs. S17, S19), no traces of a precursor carbonate or clastic fabric was observed. Hence, WF4 and PAN1-1A represent primary seafloor cherts (Sugitani et al., 2010, 2013). Early trapping by silica of hydrocarbons seeping at the seafloor would be consistent with the dark, clotted chert fabric. However, simultaneous trapping cannot explain the wide range of $\delta^{13}C_{org}$ of up to 10‰ between dense clots and globules, and the texture-specific isotopic fractionations observed in OM. If textures are controlled only by grain shape, then the $\delta^{13}C_{org}$ values would be mixed, with no correlation to texture. Moreover, the individualized, non-coalesced structure of spheres argues against accretion around spherulitic quartz. So far, no mineral shape is known to template the abiotic accretion of lenses formed by flanged lenticular structures (Sugitani et al., 2010, 2013), in particular those connected in chains by a smooth diffuse appendage (Fig. 3D).

Bitumen-bearing fluid inclusions represent another possible precursor for pyrobitumen aggregates. However, fluid inclusions have only been described that contain a small fraction of OM occurring as nanoscale oil rims (Dutkiewicz et al., 2007; George et al., 2008), which cannot explain the dense OM aggregates in clots, globules and lenses. In addition, spheres and lenses are now filled by quartz. Precursor fluid inclusions would have to collapse and leak before forming such structures. Textures characteristic of metamorphosed fluid inclusions such as necking and negative quartz crystal shapes are, however, absent in spheres and lenses. Hence, their formation from oil-bearing fluid inclusions can be ruled out.

In conclusion, there are abundant textural, structural, and geochemical features arguing against a metamorphic origin to the coupled textural-isotopic heterogeneities observed in our samples. Only micro-veins show evidence of OM migration beyond the millimeter scale, and these are demonstrably late compared to other OM-texture types, which must be indigenous to the cherts. Spheres, lenses and globules occur throughout WF4 and show no spatial relationship with the denser OM clots. Hence, in situ formation of spheres, lenses and globules by expulsion from dense kerogen clots during rapid hydrothermal alteration is unlikely. Some primary or early diagenetic OM microreservoirs, OM-textures and $\delta^{13}C_{org}$ heterogeneities may thus have been preserved in the SPF cherts, the origin of which is discussed below.

7.5. Primary $\delta^{13}C_{org}$ and H/C heterogeneities

Processes that may produce primary $\delta^{13}C_{org}$ heterogeneities include abiotic OM syntheses, metabolic fractionations, and selective preservation of biosynthetically fractionated classes of molecules. Correlated variations of $\delta^{13}C_{org}$, textures, and H/C provide valuable insights into these processes.

7.5.1. Abiotic-origin models

Abiotic Fischer–Tropsch-type (FTT) reactions can synthesize molecules with a range of ^{13}C-depletions compared to parent CO_2 similar to biological fractionations (Horita,

2005; McCollom and Seewald, 2006). These reactions may be relevant to reducing hydrothermal systems with required catalysts (metals, Fe-oxides) in mafic volcanic rocks. The presence of massive, black OM-bearing feeder veins that cut across some parts of the SPF and underlying volcanic rocks and that possibly vented in submarine hot-springs has been used to argue for an abiotic origin for all OM in the SPF (Lindsay et al., 2005). In the Goldsworthy greenstone belt (WF4, WFL2-1), no massive OM-bearing veins cut across the SPF cherts (Sugitani et al., 2010). Massive OM-bearing veins cutting across the SPF occur near the Panorama site at the Trendall Locality (Lindsay et al., 2005), but not in the outcrop where horizons of the PAN1-1A chert occur (Sugitani et al., 2013). The 3.4 Ga cherts in the Kromberg Formation (South Africa) show similar OM microstructures including lenses, and neither they nor underlying volcanic rocks are cut by massive OM-bearing veins (Walsh, 1992). Moreover, as detailed above, migration beyond the millimeter-scale cannot explain clots, globules, lenses and spheres textures in our cherts. OM forming these microstructures is thus not related to distant massive veins introducing OM throughout pre-existing cherts.

Syn-sedimentary labile molecules vented with hydrothermal fluids could be proposed to have aggregated and polymerized to shape these microstructures either: (i) in hydrothermal conduits, or (ii) upon mixing with seawater, or (iii) within seafloor cherts. First, the OM in massive veins cutting the SPF cherts and underlying volcanics is essentially clot-like, and these veins do not show spheres, lenses, or clusters of globules (Lindsay et al., 2005). It is thus unlikely that these microstructures were shaped in hydrothermal conduits before sedimentation. Second, assemblages of organic microstructures with similar carbon isotope ratios occur in the two sampled SPF sites, which are ~100 km apart and likely marked by a gap in time (Sugitani et al., 2010, 2013). This consistency of isotopic fractionation processes and precipitation mechanisms is highly unlikely at the interface between different hydrothermal vents and seawater (Marshall et al., 2007). So far, little is known about the precipitation and polymerization potentials of FTT-synthesis products once they are mixed in seawater (Marshall et al., 2007), and no insoluble residues have been reported in hydrothermal experiments (McCollom and Seewald, 2006). Rather, insoluble pyrobitumen could have formed in chert through cracking by hydrothermal metasomatism at shallow depth or during burial metamorphism (Marshall et al., 2007). In this scenario, organic molecules would migrate in the chert and concentrate at grain boundaries and each OM generation may be characterized by a distinct texture at each microstructural evolution step of the forming/recrystallizing chert. These scenarios are, however, difficult to reconcile with the wide range of $\delta^{13}C_{org}$ observed in SPF in this study and by Wacey et al. (2011) and, in particular, with the texture-specific isotopic compositions we report. Indeed, formation of distinct generations of bitumen with distinct $\delta^{13}C_{org}$ is usually caused by stepwise expulsion of specific classes of molecules bearing distinct biosynthetic isotopic fractionations (Hayes, 2001; Galimov, 2006; Close et al., 2011). Molecule-specific isotopic fractionations were not observed in non-volatile FTT-synthesis products (McCollom and Seewald, 2006). Hence, small-scale migration of specific classes of molecules is unlikely to have formed isotopically distinct generations of abiogenic bitumen at the sub-millimeter scale in the studied cherts. Therefore, we find no evidence for a mechanism simultaneously controlling quartz microstructures, fluid migrations, the $\delta^{13}C_{org}$ and the condensation of abiogenic organics. Molecule-specific $\delta^{13}C_{org}$ variation of −36‰ to −29‰ were observed in series of bound polyaromatic hydrocarbons in other SPF kerogen (Marshall et al., 2007). Textural- and molecule-specific isotopic heterogeneities may thus represent important indicators of biogenicity in such mature OM.

7.5.2. Metabolic fractionation of carbon isotopes

Assuming they are representative of the parent biomass, $\delta^{13}C_{org}$ values of each OM-texture type can be used tentatively to propose metabolic pathways. Lenses may represent microfossils of photoautotrophs using the RuBisCO pathway, chemoautotrophs using the acetyl Co-A pathway, or heterotrophic microorganisms replacing primary biomass (Pearson, 2010). Spheres show lower values of $\delta^{13}C_{org}$ consistent with microorganisms using the same metabolic pathways, but also methanogens, or methanotrophs (House et al., 2000, 2003; Pearson, 2010). Clots show a texture consistent with a polymerized residue of degraded organic matter (Lepot et al., 2009). Heterotrophic degradation increases $\delta^{13}C_{org}$ by ca. 1–2‰ (Pearson, 2010), and larger increases can be produced when several trophic levels overprint the initial biomass (Close et al., 2011). Accordingly, the bimodal distribution of $\delta^{13}C_{org}$ in clots may represent distinct trophic levels. Globules are the lowest $\delta^{13}C$ OM-texture type in WF4 and may accordingly represent biomass of heterotrophic or chemolithotrophic methanogens, methanotrophs, or sulfate reducers (House et al., 2003; Pearson, 2010). Hence, they possibly represent the final biodegradation steps in the ecosystem. Similar globule clusters in Archean cherts (Glikson et al., 2008) or carbonates (Lepot et al., 2009) were interpreted as cellular microfossils. This is supported by their size, shape, and the observation of dense OM globules during thermal alteration of pure cultures of methanotrophs (Glikson et al., 2008). However, studies of hydrothermal alteration of pure cultures did not assess the role of mineral catalysts (Hetenyi, 1995) on the preservation or formation of such globules. In addition, the aggregation of OM into dense globules is unlike most microfossils that usually display hollow structures. Alternatively, these globules may represent (individual or coalesced) dense polymeric lipid granules/droplets, which may represent up to 90% of the dry weight of some prokaryotes (Wältermann and Steinbüchel, 2005). In this case, their isotopic composition may not be representative of the bulk cells (Fig. 8B and below) and C-fixation metabolism.

7.5.3. Selective preservation of OM

PAN1-1A and WF4 show the same 10‰ range of $\delta^{13}C_{org}$ between the most ^{13}C-enriched clots and the most ^{13}C-depleted globules. This range may be accounted for by separation of classes of biomolecules from the biomass

of a single primary producer, as well as from the biomass of a complex ecosystem characterized by distinct metabolic fractionations (Hayes, 2001; Pearson, 2010). Indeed, biosynthetic processes within a cell form micro-reservoirs of molecules (Fig. 8B) with values of $\delta^{13}C_{org}$ distinct from that of the whole cell (Sakata et al., 1997; Hayes, 2001; Teece and Fogel, 2007). Distinct micro-reservoirs can be distinguished by in situ $\delta^{13}C_{org}$ analysis of well-preserved microfossils (Williford et al., 2013), as shown in Fig. 8C. These classes of molecules have distinct reactivity and timing of formation during biodegradation and fossilization (Galimov, 2006; Close et al., 2011) and may polymerize independently through early diagenetic processes such as sulfurization (Sinninghe Damste et al., 1998). Most importantly, the coupled $\delta^{13}C_{org}$–H/C heterogeneities we observed (Fig. 8A) support the conclusion that the texture-specific isotopic fractionations result from condensation and/or preservation of specific classes of molecules.

The spheres in SPF cherts are morphologically consistent with cell membranes (Fig. 8E). Accordingly, their low $\delta^{13}C_{org}$ value may represent that of selectively preserved membrane lipids, which are generally ^{13}C-depleted compared to bulk cells (Sakata et al., 1997). Similarly, globules may represent condensates of biosynthetically ^{13}C-depleted lipids separated from the fossil biomass (Sakata et al., 1997; Hayes, 2001).

Lenses partly or mostly filled by reticulated OM are morphologically consistent with preservation of a thick polysaccharide sheath or capsule. Selective polymerization of ^{13}C-enriched polysaccharides (Sinninghe Damste et al., 1998) may have raised the $\delta^{13}C_{org}$ in lenticular microfossils by a few ‰ (Fig. 8B) relative to whole precursor cells (Teece and Fogel, 2007). Within lenses, ^{13}C-depleted globules may represent (i) post-mortem condensation of membrane lipids forming the initial lenticular cells, or (ii) preservation of primary intracellular storage granules or droplets composed of lipids (Wältermann and Steinbüchel, 2005), Fig. 8B. On the one hand, the isotopic composition of membrane lipids is well known and characterized by biosynthetically ^{13}C-depleted lipids (Sakata et al., 1997; Hayes, 2001). Globular preservation of lipids could explain the difference in $\delta^{13}C_{org}$ (up to ~9‰, Fig. 8) between globular lenses and globule-free lenses. Similarly, Proterozoic microfossils display internal globules with $\delta^{13}C_{org}$ ~2.5‰ lower than their bounding wall (Fig. 8C) and were interpreted as resulting from the selective preservation of lower biosynthetic $\delta^{13}C_{org}$ of lipids in globules and higher $\delta^{13}C_{org}$ of peptidoglycan in walls (Williford et al., 2013). On the other hand, to our knowledge, little is known about the specific isotopic composition of intracellular (storage) lipid globules. Some bacteria show storage lipids composed of polyhydroxyalkanoic acids with $\delta^{13}C$ values 0.9–3‰ higher than bulk cells (van der Meer et al., 2001). In other prokaryotes, storage globules are composed of wax esters (Wältermann and Steinbüchel, 2005), a class of lipids that usually shows a lower $\delta^{13}C$ than bulk cells (Hayes, 2001; van der Meer et al., 2001). The hypothesis where low $\delta^{13}C_{org}$ globules within microfossils represent lipid granules rather than collapsed membranes requires further investigation of living cells.

8. CONCLUSIONS

This study combines petrographic analysis with in situ measurement of structural and geochemical tracers. These micrometer-scale data provide invaluable information on the origin and alteration history of one of the oldest preserved OM occurrences. For the first time, in situ analysis has revealed texture-linked structural, isotopic and H/C heterogeneities in organic microstructures of the Strelley Pool Formation. The main implications of this study are:

- OM in micro-veins shows a high H/C, a lower structural order, and a higher $\delta^{13}C_{org}$ compared to all other OM microstructures within the chert matrix they cut across. Vein OM thus likely post-dates peak metamorphism. All other OM microstructures (lenses, spheres, globules and clots) show a similar, higher structural order and pre-date peak metamorphism.
- A general positive correlation links $\delta^{13}C_{org}$ and H/C, and is most evident in globules with low $\delta^{13}C_{org}$ and low H/C compared to clots with high $\delta^{13}C_{org}$ and high H/C. This relation verifies for the first time that SIMS isotopic bias arising from variable H/C ratios is negligible for H-poor Paleoarchean OM but standards must match samples in composition and structure state. Likewise, alteration reactions with preferential loss of ^{12}C and metamorphic exchange of OM with carbonates would both produce a negative correlation of $\delta^{13}C_{org}$ and H/C, which is not seen. Hence, this relation demonstrates that sub-millimeter-scale isotopic heterogeneities within the cherts are not the sole result of heterogeneous metamorphic or metasomatic alteration from a single OM precursor. Based on negative correlations in other terranes between $\delta^{13}C_{org}$ and H/C, N/C or $\delta^{15}N$, several studies suggested that the best preserved OM in Paleoarchean cherts is that found in the lowest $\delta^{13}C_{org}$ micro- to macro-reservoirs, often with $\delta^{13}C_{org} < -36‰$ (Ueno et al., 2004; van Zuilen et al., 2007; Pinti et al., 2009a). For the in situ data of this study, the opposite relation shows that the 10‰ $\delta^{13}C_{org}$ range observed in pre-metamorphic OM in WF4 and PAN1-1A was not produced by such alteration and indicates the preservation of primary and/or diagenetic heterogeneities.
- Several lines of evidence indicate that the pre-metamorphic OM textures (clots, globules, lenses, spheres) are indigenous to the cherts and that OM could not have migrated beyond the millimeter-scale. Diagnostic textural features of radiogenic pyrobitumen and oil-bearing inclusions are absent. The texture-specific isotopic compositions and the absence of OM at the interface between pure chert regions and OM-rich chert argue against large-scale migration associated with pyrobitumen formation. These results also rule out a pervasive migration of hydrocarbons from intrusive hydrothermal veins into pre-existing chert as the origin of lenses, spheres, clots and globules. Moreover, texture-specific isotopic and H/C heterogeneities argue against an abiotic hydrothermal origin for OM within the SPF cherts.

– The 10‰ range of $\delta^{13}C_{org}$ in indigenous OM of both PAN1-1A and WF4 is consistent with a complex microbial food chain. However, such $\delta^{13}C_{org}$ heterogeneities can also be partly to fully explained by selective preservation and diagenetic polymerization processes. Selective preservation is crucial in the fossilization of cellular structures (Vandenbroucke and Largeau, 2007). The narrow range of isotopic values recorded in spheres and lenses is consistent with the narrow ranges recorded in fresh bacterial monocultures (Orphan and House, 2009) and in microfossils (House et al., 2000; Kaufman and Xiao, 2003; Orphan and House, 2009; Williford et al., 2013). Specifically, the $\delta^{13}C_{org}$ distribution of spheres displays a sharp peak at values distinct from lenses, but also from recondensed OM such as clots, globules and micro-veins. This supports selective preservation of specific classes of macromolecules in spheres, as opposed to condensation of polymers from degraded biomass. Isotopic differences between the OM network that forms lenses and their internal globules are similar to isotopic heterogeneities preserved within Proterozoic microfossils (Williford et al., 2013). Hence, $\delta^{13}C_{org}$ values support the conclusion that spheres and lenses are microfossils.

ACKNOWLEDGEMENTS

We thank Noriko Kita, Jim Kern and Kouki Kitajima for assistance with SIMS analyses, Brian Hess for expert SIMS mount preparation, Tsutomu Nagaoka for thin section preparation, Christopher House (Penn State University) for providing the PPRG215-1 standard, Myriam Moreau for assistance with Raman analyses, and Sandra Ventalon for assistance with CL imaging. We thank A. Nemchin (associate editor) and two anonymous reviewers for constructive comments. Funding was provided by the NASA Astrobiology Institute. The WiscSIMS Lab is partially funded by NSF-EAR (0319230, 0744079, 1053466). Kenichiro Sugitani was funded by Japan Society for Promotion of Science (Nos. 22340149 and 24654162). Raman analyses were funded by CNRS-INSU INTERRVIE (K.L.).

APPENDIX A. SUPPLEMENTARY DATA

Supplementary data associated with this article can be found, in the online version, at http://dx.doi.org/10.1016/j.gca.2013.03.004.

REFERENCES

Allwood A. C., Walter M. R., Kamber B. S., Marshall C. P. and Burch I. W. (2006a) Stromatolite reef from the Early Archaean era of Australia. *Nature* **441**, 714–718.

Allwood A. C., Walter M. R. and Marshal C. P. (2006b) Raman spectroscopy reveals thermal palaeoenvironments of c.3.5 billion-year-old organic matter. *Vib. Spectrosc.* **41**, 190–197.

Allwood A. C., Grotzinger J. P., Knoll A. H., Burch I. W., Anderson M. S., Coleman M. L. and Kanik I. (2009) Controls on development and diversity of Early Archean stromatolites. *Proc. Natl. Acad. Sci. U.S.A.* **106**, 9548–9555.

Allwood A. C., Kamber B. S., Walter M. R., Burch I. W. and Kanik I. (2010) Trace elements record depositional history of an Early Archean stromatolitic carbonate platform. *Chem. Geol.* **270**, 148–163.

Aoya M., Kouketsu Y., Endo S., Shimizu H., Mizukami T., Nakamura D. and Wallis S. (2010) Extending the applicability of the Raman carbonaceous-material geothermometer using data from contact metamorphic rocks. *J. Metamorph. Geol.* **28**, 895–914.

Bernard S., Benzerara K., Beyssac O. and Brown G. E. (2010a) Multiscale characterization of pyritized plant tissues in blueschist facies metamorphic rocks. *Geochim. Cosmochim. Acta* **74**, 5054–5068.

Bernard S., Beyssac O., Benzerara K., Findling N., Tzvetkov G. and Brown G. E. (2010b) XANES, Raman and XRD study of anthracene-based cokes and saccharose-based chars submitted to high-temperature pyrolysis. *Carbon* **48**, 2506–2516.

Beyssac O., Goffe B., Chopin C. and Rouzaud J. N. (2002) Raman spectra of carbonaceous material in metasediments: a new geothermometer. *J. Metamorph. Geol.* **20**, 859–871.

Beyssac O., Goffe B., Petitet J. P., Froigneux E., Moreau M. and Rouzaud J. N. (2003) On the characterization of disordered and heterogeneous carbonaceous materials by Raman spectroscopy. *Spectrochim. Acta Part A – Mol. Biomol. Spectrosc.* **59**, 2267–2276.

Bontognali T. R. R., Sessions A. L., Allwood A. C., Fischer W. W., Grotzinger J. P., Summons R. E. and Eiler J. M. (2012) Sulfur isotopes of organic matter preserved in 3.45-billion-year-old stromatolites reveal microbial metabolism. *Proc. Natl. Acad. Sci. U.S.A.* **109**, 15146–15151.

Brasier M. D., Green O. R., Jephcoat A. P., Kleppe A. K., Van Kranendonk M. J., Lindsay J. F., Steele A. and Grassineau N. V. (2002) Questioning the evidence for Earth's oldest fossils. *Nature* **416**, 76–81.

Brasier M. D., Green O. R., Lindsay J. F., McLoughlin N., Steele A. and Stoakes C. (2005) Critical testing of earth's oldest putative fossil assemblage from the similar to 3.5 Ga Apex Chert, Chinaman Creek, western Australia. *Precambrian Res.* **140**, 55–102.

Buick R. (1990) Microfossil recognition in Archean rocks: an appraisal of spheroids and filaments from a 3500 m.y. old chert-barite unit at North Pole, Western Australia. *Palaios* **5**, 441–459.

Buick R., Rasmussen B. and Krapez B. (1998) Archean oil: evidence for extensive hydrocarbon generation and migration 2.5–3.5 Ga. *AAPG Bull.* **82**, 50–69.

Close H. G., Bovee R. and Pearson A. (2011) Inverse carbon isotope patterns of lipids and kerogen record heterogeneous primary biomass. *Geobiology* **9**, 250–265.

Derenne S., Robert F., Skrzypczak-Bonduelle A., Gourier D., Binet L. and Rouzaud J. N. (2008) Molecular evidence for life in the 3.5 billion year old Warrawoona chert. *Earth Planet. Sci. Lett.* **272**, 476–480.

Des Marais D. J. (2001) Isotopic evolution of the biogeochemical carbon cycle during the Precambrian. In *Reviews In Mineralogy and Geochemistry, vol 43: Stable Isotope Geochemistry* (eds. J. W. Valley and D. R. Cole). Mineralogical Society of America.

Dunn S. R. and Valley J. W. (1992) Calcite–graphite isotope thermometry: a test for polymetamorphism in marble, Tudor Gabbro aureole, Ontario. *J. Metamorph. Geol.* **10**, 487–501.

Dutkiewicz A., George S. C., Mossman D. J., Ridley J. and Volk H. (2007) Oil and its biomarkers associated with the Palaeoproterozoic Oklo natural fission reactors, Gabon. *Chem. Geol.* **244**, 130–154.

Ferry J. M., Ushikubo T., Kita N. T. and Valley J. W. (2010) Assessment of grain-scale homogeneity and equilibration of carbon and oxygen isotope compositions of minerals in

carbonate-bearing metamorphic rocks by ion microprobe. *Geochim. Cosmochim. Acta* **74**, 6517–6540.

Galimov E. M. (2006) Isotope organic geochemistry. *Org. Geochem.* **37**, 1200–1262.

Garcia-Ruiz J. M., Hyde S. T., Carnerup A. M., Christy A. G., Van Kranendonk M. J. and Welham N. J. (2003) Self-assembled silica-carbonate structures and detection of ancient microfossils. *Science* **302**, 1194–1197.

George S. C., Volk H., Dutkiewicz A., Ridley J. and Buick R. (2008) Preservation of hydrocarbons and biomarkers in oil trapped inside fluid inclusions for >2 billion years. *Geochim. Cosmochim. Acta* **72**, 844–870.

Glikson M., Duck L. J., Golding S. D., Hofmann A., Bolhar R., Webb R., Baiano J. C. F. and Sly L. I. (2008) Microbial remains in some earliest Earth rocks: comparison with a potential modern analogue. *Precambrian Res.* **164**, 187–200.

Grey K. and Sugitani K. (2009) Palynology of Archean microfossils (c. 3.0 Ga) from the Mount Grant area, Pilbara Craton, Western Australia: further evidence of biogenicity. *Precambrian Res.* **173**, 60–69.

Hayes J. M., Kaplan I. R. and Wedeking K. W. (1983) Precambrian organic geochemistry, preservation of the record. In *The Earth's Earliest Biosphere* (ed. J. W. Schopf). Princeton University Press, Princeton, New Jersey.

Hayes J. M. (2001) Fractionation of carbon and hydrogen isotopes in biosynthetic processes. In *Stable Isotope Geochemistry* (eds. J. W. Valley and D. Cole). Mineralogical Society of America.

Hetenyi M. (1995) Simulated thermal maturation of type-I and type-III kerogens in the presence, and absence, of calcite and montmorillonite. *Org. Geochem.* **23**, 121–127.

Hickman, A. H. (2008) *Regional review of the 3426–3350Ma Strelley Pool Formation, Pilbara Craton, Western Australia. Geological Survey of Western Australia, Record 2008/15*.

Horita J. (2005) Some perspectives on isotope biosignatures for early life. *Chem. Geol.* **218**, 171–186.

House C. H., Schopf J. W., McKeegan K. D., Coath C. D., Harrison T. M. and Stetter K. O. (2000) Carbon isotopic composition of individual Precambrian microfossils. *Geology* **28**, 707–710.

House C. H., Schopf J. W. and Stetter K. O. (2003) Carbon isotopic fractionation by Archaeans and other thermophilic prokaryotes. *Org. Geochem.* **34**, 345–356.

Javaux E. J., Marshal C. P. and Bekker A. (2010) Organic-walled microfossils in 3.2-billion-year-old shallow-marine siliciclastic deposits. *Nature* **463**, 934–938.

Jehlička J., Urban O. and Pokorny J. (2003) Raman spectroscopy of carbon and solid bitumens in sedimentary and metamorphic rocks. *Spectrochim. Acta Part A – Mol. Biomol. Spectrosc.* **59**, 2341–2352.

Kaufman A. J. and Xiao S. (2003) High CO_2 levels in the Proterozoic atmosphere estimated from analyses of individual microfossils. *Nature* **425**, 279–282.

Kazmierczak J. and Kremer B. (2009) Thermally altered silurian cyanobacterial mats: a key to Earth's oldest fossils. *Astrobiology* **9**, 731–743.

Kita N. T., Ushikubo T., Fu B. and Valley J. W. (2009) High precision SIMS oxygen isotope analysis and the effect of sample topography. *Chem. Geol.* **264**, 43–57.

Kitchen N. E. and Valley J. W. (1995) Carbon isotope thermometry in marbles of the Adirondack Mountains, New York. *J. Metamorph. Geol.* **13**, 577–594.

Lahfid A., Beyssac O., Deville E. F. N., Chopin C. and Goffé B. (2010) Evolution of the Raman spectrum of carbonaceous material in low-grade metasediments of the Glarus Alps (Switzerland). *Terra Nova* **22**, 354–360.

Lepot K., Benzerara K., Brown G. E. and Philippot P. (2008) Microbially influenced formation of 2724 million years old stromatolites. *Nat. Geosci.* **1**, 118–121.

Lepot K., Benzerara K., Rividi N., Cotte M., Brown G. E. and Philippot P. (2009) Organic matter heterogeneities in 2.72 Ga stromatolites: alteration versus preservation by sulphur incorporation. *Geochim. Cosmochim. Acta* **73**, 6579–6599.

Lindsay J. F., Brasier M. D., McLoughlin N., Green O. R., Fogel M., Steele A. and Mertzman S. A. (2005) The problem of deep carbon – an Archean paradox. *Precambrian Res.* **143**, 1–22.

Marshall C. P., Love G. D., Snape C. E., Hill A. C., Allwood A. C., Walter M. R., Van Kranendonk M. J., Bowden S. A., Sylva S. P. and Summons R. E. (2007) Structural characterization of kerogen in 3.4 Ga Archaean cherts from the Pilbara Craton, Western Australia. *Precambrian Res.* **155**, 1–23.

Marshall C. P., Emry J. R. and Olcott Marshall A. (2011) Haematite pseudomicrofossils present in the 3.5-billion-year-old Apex Chert. *Nat. Geosci.* **4**, 240–243.

McCollom T. M. and Seewald J. S. (2006) Carbon isotope composition of organic compounds produced by abiotic synthesis under hydrothermal conditions. *Earth Planet. Sci. Lett.* **243**, 74–84.

McLoughlin N., Grosch E. G., Kilburn M. R. and Wacey D. (2012) Sulfur isotope evidence for a Paleoarchean subseafloor biosphere, Barberton, South Africa. *Geology* **40**, 1031–1034.

Oehler D. Z., Robert F., Mostefaoui S., Meibom A., Selo M. and McKay D. S. (2006) Chemical mapping of proterozoic organic matter at submicron spatial resolution. *Astrobiology* **6**, 838–850.

Oehler D. Z., Robert F., Walter M. R., Sugitani K., Meibom A., Mostefaoui S. and Gibson E. K. (2010) Diversity in the archean biosphere: new Insights from NanoSIMS. *Astrobiology* **10**, 413–424.

Olcott Marshall A., Emry J. R. and Marshall C. P. (2012) Multiple generations of carbon in the apex chert and implications for preservation of microfossils. *Astrobiology* **12**, 160–166.

Orphan V. J. and House C. H. (2009) Geobiological investigations using secondary ion mass spectrometry: microanalysis of extant and paleo-microbial processes. *Geobiology* **7**, 360–372.

Papineau D., Gregorio B. T. D., Cody G. D., Fries M. D., Mojzsis S. J., Steele A., Stroud R. M. and Fogel M. L. (2010) Ancient graphite in the Eoarchean quartz–pyroxene rocks from Akilia in southern West Greenland I: petrographic and spectroscopic characterization. *Geochim. Cosmochim. Acta* **74**, 5884–5905.

Pearson A. (2010) Pathways of carbon assimilation and their impact on organic matter values $d^{13}C$. In *Handbook of Hydrocarbon and Lipid Microbiology* (ed. K. N. Timmis). Springer-Verlag, Berlin Heidelberg.

Philippot P., Van Zuilen M., Lepot K., Thomazo C., Farquhar J. and Van Kranendonk M. (2007) Early Archaean microorganisms preferred reduced sulfur, not sulfate. *Science* **317**, 1534–1537.

Philippot P., Zuilen M. v. and Rollion-Bard C. (2012) Variations in atmospheric sulphur chemistry on early Earth linked to volcanic activity. *Nat. Geosci.* **5**, 668–674.

Pinti D. L., Hashizume K., Sugihara A., Massault M. and Philippot P. (2009a) Isotopic fractionation of nitrogen and carbon in Paleoarchean cherts from Pilbara craton, Western Australia: origin of 15N-depleted nitrogen. *Geochim. Cosmochim. Acta* **73**, 3819–3848.

Pinti D. L., Mineau R. and Clement V. (2009b) Hydrothermal alteration and microfossil artefacts of the 3465-million-year-old Apex chert. *Nat. Geosci.* **2**, 640–643.

Quirico E., Montagnac G., Rouzaud J.-N., Bonal L., Bourot-Denise M., Duber S. and Reynard B. (2009) Precursor and metamorphic condition effects on Raman spectra of poorly

ordered carbonaceous matter in chondrites and coals. *Earth Planet. Sci. Lett.* **287**, 185–193.

Riciputi L. R. and Greenwood J. P. (1998) Analysis of sulfur and carbon isotope ratios in mixed matrices by secondary ion mass spectrometry: implications for mass bias corrections. *Int. J. Mass Spectrom.* **178**, 65–71.

Sakata S., Hayes J. M., McTaggart A. R., Evans R. A., Leckrone K. J. and Togasaki R. K. (1997) Carbon isotopic fractionation associated with lipid biosynthesis by a cyanobacterium: relevance for interpretation of biomarker records. *Geochim. Cosmochim. Acta* **61**, 5379–5389.

Sangély L., Chaussidon M., Michels R. and Huault V. (2005) Microanalysis of carbon isotope composition in organic matter by secondary ion mass spectrometry. *Chem. Geol.* **223**, 179–195.

Sangély L., Chaussidon M., Michels R., Brouand M., Cuney M., Huault V. and Landais P. (2007) Micrometer scale carbon isotopic study of bitumen associated with Athabasca uranium deposits: constraints on the genetic relationship with petroleum source-rocks and the abiogenic origin hypothesis. *Earth Planet. Sci. Lett.* **258**, 378–396.

Schopf J. W. (1993) Microfossils of the Early Archean Apex Chert – new evidence of the antiquity of life. *Science* **260**, 640–646.

Schopf J. W. and Kudryavtsev A. B. (2012) Biogenecity of Earth's earliest fossils: a resolution of the controversy. *Gondowana Res.* **22**, 761–771.

Schopf J. W., Kudryavtsev A. B., Agresti D. G., Wdowiak T. J. and Czaja A. D. (2002) Laser-Raman imagery of Earth's earliest fossils. *Nature* **416**, 73–76.

Schopf J. W., Kudryavtsev A. B., Sugitani K. and Walter M. R. (2010) Precambrian microbe-like pseudofossils: a promising solution to the problem. *Precambrian Res.* **179**, 191–205.

Shen Y., Farquhar J., Masterson A., Kaufman A. J. and Buick R. (2009) Evaluating the role of microbial sulfate reduction in the early Archean using quadruple isotope systematics. *Earth Planet. Sci. Lett.* **279**, 383–391.

Sherwood Lollar B. and McCollom T. M. (2006) Biosignatures and abiotic constraints on early life (Communications arising). *Nature* **444**, E18.

Sinninghe Damste J. S., Kok M. D., Koster J. and Schouten S. (1998) Sulfurized carbohydrates: an important sedimentary sink for organic carbon? *Earth Planet. Sci. Lett.* **164**, 7–13.

Sugitani K., Grey K., Allwood A., Nagaoka T., Mimurae K., Minami M., Marshall C. P., Kranendonk M. J. V. and Walter M. R. (2007) Diverse microstructures from Archaean chert from the Mount Goldsworthy–Mount Grant area, Pilbara Craton, Western Australia: microfossils, dubiofossils, or pseudofossils? *Precambrian Res.* **158**, 228–262.

Sugitani K., Lepot K., Nagaoka T., Mimura K., Kranendonk M. V., Oehler D. Z. and Walter M. R. (2010) Biogenicity of morphologically diverse carbonaceous microstructures from the ca. 3400 Ma Strelley Pool Formation, in the Pilbara Craton, Western Australia. *Astrobiology* **10**, 899–920.

Sugitani K., Mimura K., Nagaoka T., Lepot K. and Takeuchi M. (2013) Microfossil assemblage from the 3400 Ma Strelley Pool Formation in the Pilbara Craton, Western Australia: results form a new locality. *Precambrian Res.* **226**, 59–74.

Teece M. A. and Fogel M. L. (2007) Stable carbon isotope biogeochemistry of monosaccharides in aquatic organisms and terrestrial plants. *Org. Geochem.* **38**, 458–473.

Tice M. M. and Lowe D. R. (2006) The origin of carbonaceous matter in pre-3.0 Ga greenstone terrains: a review and new evidence from the 3.42 Ga Buck Reef Chert. *Earth. Sci. Rev.* **76**, 259–300.

Tice M. M., Bostick B. C. and Lowe D. R. (2004) Thermal history of the 3.5-3.2 Ga Onverwacht and Fig Tree Groups, Barberton greenstone belt, South Africa, inferred by Raman microspectroscopy of carbonaceous material. *Geology* **32**, 37–40.

Ueno Y., Isozaki Y., Yurimoto H. and Maruyama S. (2001) Carbon isotopic signatures of individual archean microfossils(?) from Western Australia. *Int. Geol. Rev.* **43**, 196–212.

Ueno Y., Yoshioka H., Maruyama S. and Isozaki Y. (2004) Carbon isotopes and petrography of kerogens in ~3.5-Ga hydrothermal silica dikes in the North Pole area, Western Australia. *Geochim. Cosmochim. Acta* **68**, 573–589.

Ueno Y., Yamada K., Yoshida N., Maruyama S. and Isozaki Y. (2006a) Evidence from fluid inclusions for microbial methanogenesis in the early Archaean era. *Nature* **440**, 516–519.

Ueno Y., Yamada K., Yoshida N., Maruyama S. and Isozaki Y. (2006b) Reply to "Biosignatures and abiotic constraints on early life". *Nature* **444**, E18–19.

Ueno Y., Ono S., Rumble D. and Maruyama S. (2008) Quadruple sulfur isotope analysis of ca. 3.5 Ga Dresser Formation: new evidence for microbial sulfate reduction in the early Archean. *Geochim. Cosmochim. Acta* **72**, 5675–5691.

Valley, J. W. (2001). Reviews in mineralogy and geochemistry, vol. 43: stable isotope thermometry at high temperatures. In *Stable Isotope Geochemistry* (eds. J. W. Valley and D. R. Cole). Mineralogical Society of America, Chantilly, Virginia.

Valley, J. W. and Kita, N. T. (2009). In situ Oxygen Isotope Geochemistry by Ion Microprobe. In *MAC Short Course, vol. 41: Secondary Ion Mass Spectrometry in the Earth Sciences* (ed. M. Fayek). Mineralogical Association of Canada, Toronto, Ontario.

van der Meer M. T. J., Schouten S., van Dongen B. E., Rijpstra W. I. C., Fuchs G., Sinninghe Damsté J. S., de Leeuw J. W. and Ward D. M. (2001) Biosynthetic controls on the 13C contents of organic components in the photoautotrophic bacterium *Chloroflexus aurantiacus*. *J. Biol. Chem.* **276**, 10971–10976.

van Zuilen M. A., Chaussidon M., Rollion-Bard C. and Marty B. (2007) Carbonaceous cherts of the Barberton Greenstone Belt, South Africa: isotopic, chemical and structural characteristics of individual microstructures. *Geochim. Cosmochim. Acta* **71**, 655–669.

van Zuilen M. A., Fliegel D., Wirth R., Lepland A., Qu Y., Schreiber A., Romashkin A. E. and Philippot P. (2012) Mineral-templated growth of natural graphite films. *Geochim. Cosmochim. Acta* **83**, 252–262.

Vandenbroucke M. and Largeau C. (2007) Kerogen origin, evolution and structure. *Org. Geochem.* **38**, 719–833.

Wacey D., McLoughlin N., Whitehouse M. J. and Kilburn M. R. (2010) Two coexisting sulfur metabolisms in a ca. 3400 Ma sandstone. *Geology* **38**, 1115–1118.

Wacey D., Kilburn M. R., Saunders M., Cliff J. and Brasier M. D. (2011) Microfossils of sulphur-metabolizing cells in 3.4-billion-year-old rocks of Western Australia. *Nat. Geosci.* **4**, 698–702.

Wacey D., Menon S., Green L., Gerstmann D., Kong C., Mcloughlin N., Saunders M. and Brasier M. (2012) Taphonomy of very ancient microfossils from the ~3400 Ma Strelley Pool Formation and ~1900 Ma Gunflint Formation: New insights using a focused ion beam. *Precambrian Res.* **220–221**, 234–250.

Walsh M. M. (1992) Microfossils and possible microfossils from the Early Archean Onverwacht Group, Barberton Mountain Land, South-Africa. *Precambrian Res.* **54**, 271–293.

Walter M. R., Hofmann H. J. and Schopf J. W. (1983) Geographic and geologic data for processed rock samples. In *Earth's Earliest Biosphere: Its Origin and Evolution* (ed. J. W. Schopf). Princeton University Press, Princeton, NJ.

Wältermann M. and Steinbüchel A. (2005) neutral lipid bodies in prokaryotes: recent insights into structure, formation, and

relationship to eukaryotic lipid depots. *J. Bacteriol.* **187**, 3607–3619.

Williford K. H., Grice K., Logan G. A., Chen J. and Huston D. (2011a) The molecular and isotopic effects of hydrothermal alteration of organic matter in the Paleoproterozoic McArthur River Pb/Zn/Ag ore deposit. *Earth Planet. Sci. Lett.* **301**, 382–392.

Williford, K. H., Ushikubo, T., Lepot, K., Hallmann, C., Spicuzza, M. J., Eigenbrode, J. L., Summons, R. E. and Valley, J. W. (2011b). In situ carbon isotope analysis of Archean organic matter with SIMS. *AGU Fall Meeting 2011*, abstract B21E–0323.

Williford K. H., Ushikubo T., Schopf J. W., Lepot K., Kitajima K. and Valley J. W. (2013) Preservation and detection of microstructural and taxonomic correlations in the carbon isotopic compositions of individual Precambrian microfossils. *Geochim. Cosmochim. Acta* **104**, 165–182.

Yamaguchi T., Senda R., Sugitani K., Mimura K., Ueno S. and Suzuki K. (2011) *Trace elements of stromatolitic, and microfossil-bearing massive and laminated cherts from the Strelley Pool Formation*. Japan Geosci. Union Meet..

Associate editor: Alexander Nemchin